AGU PUBLICATIONS

JGR

Journal of Geophysical Research: Space Physics

RESEARCH ARTICLE
10.1002/2016JA023126

Key Points:
- Equatorial plasma and field moments in the core region are modulated at the SKR period
- The peak phase of observed plasma properties depends on the location of measurement
- Periodic changes in the magnetosphere can be described as spinning, breathing, and flapping

Supporting Information:
- Supporting Information S1
- Movie S1
- Figure S1

Correspondence to:
K. M. Ramer,
kramer@igpp.ucla.edu

Citation:
Ramer, K. M., M. G. Kivelson, N. Sergis, K. K. Khurana, and X. Jia (2017), Spinning, breathing, and flapping: Periodicities in Saturn's middle magnetosphere, *J. Geophys. Res. Space Physics*, *122*, 393–416, doi:10.1002/2016JA023126.

Received 29 JUN 2016
Accepted 28 NOV 2016
Accepted article online 5 DEC 2016
Published online 21 JAN 2017

Spinning, breathing, and flapping: Periodicities in Saturn's middle magnetosphere

K. M. Ramer[1], M. G. Kivelson[1,2], N. Sergis[3], K. K. Khurana[1], and X. Jia[2]

[1]Department of Earth, Planetary, and Space Sciences, University of California, Los Angeles, California, USA, [2]Department of Climate and Space Sciences and Engineering, University of Michigan, Ann Arbor, Michigan, USA, [3]Office for Space Research and Technology, Academy of Athens, Athens, Greece

Abstract In Saturn's magnetosphere, ubiquitous fluctuations with a period of ~10.7 h have been observed in Saturn kilometric radiation (SKR), auroral emissions, the magnetic field, the electron density, and energetic particle fluxes. Here we characterize previously unstudied periodicities in plasma properties inside of 15 R_S near the equatorial plane. Although periodically varying magnetic perturbations rotate relatively smoothly (*spinning*), plasma properties do not. The phase of the peak value of plasma density or pressure perturbations can change substantially across a few hours of local time or R_S. As a means of interpreting observations, we use a magnetohydrodynamic simulation that generates field-aligned currents centered at 70° invariant latitude in Saturn's southern ionosphere and rotating at the SKR period. The simulation reproduces many periodic features of the data including not only spinning perturbations but also global-scale compression and expansion (*breathing*). Simulated plasma properties are also modulated by periodic large-scale north-south motion (*flapping*) in regions beyond ~15 Saturn radii (R_S), which we do not analyze here. Inside of 15 R_S, plasma responds to a superposition of spinning and breathing at the spin period, developing perturbations that peak at different phases depending on what is measured and where. Strong compressional effects act impulsively over a limited range of rotation phase. Superposition of local and global-scale variations produces phase jumps across short distances and can introduce multiple peaks in the variation of plasma properties within one rotation period, accounting for anomalies in the phase dependence of periodic fluctuations identified in the sparse data available.

1. Introduction

Periodicities in magnetic and plasma properties attributable to a tilt between the spin axis and magnetic dipole axis are observed at both Earth and Jupiter. Unlike Jupiter and Earth, Saturn has an internal magnetic field that is remarkably axisymmetric; the tilt of the dipole axis is no larger than 0.06° [*Cao et al.*, 2011]. Correspondingly, one might not expect Saturn's magnetosphere to exhibit diurnal periodicities. Strangely, periodicities near the planetary rotation period (varying between 10.6 and 10.8 h) in the radio frequency power, the magnetic field, and plasma phenomena are evident throughout Saturn's magnetosphere [*Carbary and Mitchell*, 2013].

Periodicities in Saturn's kilometric radiation (SKR) were originally observed in the Voyager era [*Kaiser et al.*, 1980; *Desch and Kaiser*, 1981; *Warwick et al.*, 1981]. Voyager's measurement of the SKR showed an enhancement in power with an average period of 10 h 39 min 22 s, which was adopted by the International Astronomical Union as Saturn's internal rotation period. However, measurements with Ulysses and, later, Cassini, showed that the SKR period was changing on the order of ~1% per year, shattering the notion that the oscillation was tied to the internal rotation of the planet [*Gurnett et al.*, 2005; *Kurth et al.*, 2007, 2008]. Even more puzzlingly, analysis shows that emissions from the northern and southern hemispheres are modulated at different periods [*Gurnett et al.*, 2009a].

Periodicities at the SKR frequency have also been observed in auroral hiss [*Gurnett et al.*, 2009b], ultraviolet (UV) auroral emissions [*Nichols et al.*, 2010a, 2010b; *Provan et al.*, 2009b; *Carbary*, 2013], north-south displacement of the equatorial current sheet [*Khurana et al.*, 2009; *Arridge et al.*, 2011] (commonly referred to as *flapping*), energetic electron and neutral atom fluxes [*Carbary et al.*, 2008, 2009; *Paranicas et al.*, 2005b], the location of the magnetopause [*Clarke et al.*, 2006, 2010a, 2010b; *Pilkington et al.*, 2015], and the plasma electron density [*Gurnett et al.*, 2007]. The changing location of the magnetopause is associated with periodic global-scale compression and expansion, a feature that is well represented in the magnetohydrodynamic

simulations of *Jia et al*. [2012] and *Jia and Kivelson* [2012]. We refer to this expansion and contraction of the large portions of the magnetosphere as *breathing*, even though the term is inexact because the change of scale is not simultaneous throughout the system.

Perturbations in the magnetic field are also well organized by the SKR period [*Southwood and Kivelson*, 2007; *Andrews et al*., 2008; *Provan et al*., 2011, 2012]. In the core magnetosphere (the dipolar and quasi-dipolar equatorial region inside of 12–15 R_S), the magnetic perturbations rotate almost rigidly, so we allude to their periodic variation as *spinning*. The azimuthal perturbations of the magnetic field lag the radial perturbations by 90°. When organized by the southern SKR period, the radial and colatitudal perturbations exhibit an in-phase modulation. When organized by the northern SKR period, the radial and colatitudal perturbations are out of phase [*Andrews et al*., 2008; *Provan et al*., 2009a]. Neither the azimuthal nor radial perturbations of the magnetic field vanish at the magnetic equator [*Southwood and Kivelson*, 2007].

Periodicities of ion plasma moments in the middle magnetosphere have not been previously reported. In this study we analyze plasma parameters in Saturn's ring current region using data obtained between October 2005 and June 2006 from 6 to 15 R_S and very close to the equator to determine if plasma pressure and ion density perturbations are organized by the SKR period, as are magnetic perturbations. We find that the equatorial plasma density and pressure vary periodically within 15 R_S, but the perturbations do not remain at the same phase relative to the magnetic perturbations across all radial and local time locations. We use the simulation by *Jia et al*. [2012] to help us interpret the observed periodicities in the middle magnetosphere, finding that they arise from a superposition of two types of periodic responses to a single driver, spinning and breathing. The combined responses produce waveforms that are periodic but not sinusoidal, in some cases having multiple peaks and troughs over one 10.8 h cycle.

In section 2 we introduce the magnetic field and plasma data and the simulation. In section 3, we show the results of our analysis, extracting averages of the periodic variations of measured plasma and field properties in selected radial (r) and, where appropriate, local time (LT) bins, comparing the structure of the periodic variations in different bins to each other and to periodicities found in the simulation. In section 4, we use the simulation to understand the relationships observed in the data. Finally, we summarize our work and present the conclusions in section 5.

2. Selection and Processing of Data

Our objective is to characterize and interpret periodicities of plasma properties near the equator in Saturn's middle magnetosphere. In this section, we briefly introduce the longitude system used in this study and then discuss the field and plasma instruments and how we obtain the parameters of interest. Next, we explain why we restrict our study to the quasi-dipolar equatorial region of Saturn's middle magnetosphere. Then, we acknowledge aliasing introduced by the spatial distribution of spacecraft orbits, discuss its implications for our analysis, and bin the data into radial bins. Finally, we use the simulation of *Jia et al*. [2012] to suggest how the periodic variations of plasma properties are likely to vary with local time (LT). Breaking up the data in LT bins suggested by the simulation allows us to interpret some puzzling features of plasma pressure and density variations.

2.1. Phase System

Critical to our analysis is the local time-corrected SKR phase of each measurement. Several longitude systems have been developed based on the periodicity of SKR radiation. We use the Saturnian Longitude System 4 [*Gurnett et al*., 2011], which has both northern (valid from 5 April 2006 to 13 January 2011) and southern (valid from 12 September 2004 to 3 August 2011) components. During the interval used in this study, the northern hemisphere SKR was modulated at approximately 10.6 h; the southern hemisphere SKR, associated with magnetic perturbations roughly 3 times greater than those at the northern period [*Provan et al*., 2011], was modulated near 10.8 h and was very stable. The lower frequency (dominant) component of periodicity of SKR power between 12 September 2004 and 15 October 2009 was used to establish the SLS4-S longitude system, which we use to organize the plasma data. In the SLS4 system, the peak of SKR power occurs when the Sun is at a longitude of 100°. Other phase systems [*Lamy*, 2010; *Provan et al*., 2009a; *Andrews et al*., 2010a] define 0° as the direction toward which the magnetic perturbation vector points when the SKR power peaks. Therefore, there is a phase difference between the SLS4 phase system and that of Lamy, Provan, and Andrews. In

analyzing the data, we use the Doppler-shifted SLS4 S phase, which corrects the SLS4-S phase for the LT position of the Cassini Orbiter, as described in *Kurth et al*. [2008], with the acknowledgment that the northern signal adds jitter [*Provan et al*., 2011]. The correction for the spacecraft LT is imposed because there is evidence that the magnetic perturbation is nearly fixed in a rotating system. We refer to this LT-corrected parameter as "rotation phase." Each data point described below was assigned a rotation phase based on the SLS4-S system [*Gurnett et al*., 2011].

2.2. Data Selection

Our study uses data from plasma and field instruments aboard the Cassini spacecraft obtained when the spacecraft was in the equatorial region of Saturn's magnetosphere ($-0.5° <$ latitude $< 0.5°$) between 6 and 15 Saturn radii (R_S). The plasma parameters are provided by two instruments: the Charge Energy Mass Spectrometer (CHEMS) and Low Energy Magnetospheric Measurement System (LEMMS) sensors of the Magnetospheric Imaging Instrument (MIMI) [*Krimigis et al*., 2004] and the ion mass spectrometer (IMS) part of the CAssini Plasma Spectrometer (CAPS) [*Young et al*., 2004]. The CHEMS sensor measures energetic ions between 3 and 220 keV/*e*, while the IMS instrument samples the thermal plasma properties between 1 eV/*e* and 50 keV/*e*. The energy ranges of the CAPS and MIMI ion sensors overlap between 3 and 50 keV, but the overestimation of the plasma pressures due to this overlap is $<25\%$, well within the scatter in the data [*Sergis et al*., 2007]. The CAPS moments were calculated based on numerical integration of the observed IMS singles count rates for times when the nominal plasma corotation flow direction was in the field of view of the IMS [*Thomsen et al*., 2010]. We included only verified data with no flags, thereby limiting our number of available measurements to 950 points. Hot ion density and pressure data at 5 min resolution for ≥ 3 keV protons (H^+) and water group ions (W^+) were derived from MIMI/CHEMS and LEMMS data by integration over the energy range from 3 keV to >200 keV [*Krimigis et al*., 2004; *Sergis et al*., 2007, 2009]. The densities of H^+, He^+, and water group ions (W^+) were summed in order to obtain ion density. The contribution to the pressure from the thermal ions was calculated from temperature and density. Electron pressures in the inner equatorial magnetosphere are lower than ion pressures by a factor of 10 [*Sergis et al*., 2010] and well within the scatter in the ion observations. Consequently, electron pressures were not included in our analysis of the total pressure. Pressures derived from the CAPS and MIMI instruments are summed in order to determine total plasma pressure. We use 1 min averaged magnetic field data from the fluxgate magnetometer on the MAG instrument [*Dougherty et al*., 2004] in order to calculate magnetic pressure. All data were downloaded from the Planetary Data System (PDS).

2.3. Magnetic Pressure

Figure 1 shows the magnetic field data returned from a typical periapsis pass on one of the orbits analyzed. Figure 1 (top) shows the theta component of the magnetic field in KRTP spherical polar coordinates. The KRTP coordinate system is a planet-centered spherical system referenced to Saturn's northern spin (also magnetic field) axis. Figure 1 (middle) contains (dB_θ), the residual of the B_θ component of the magnetic field, i.e., the difference between the measured B_θ and the Cassini Saturn Orbit Insertion (SOI) magnetic field model [*Dougherty et al*., 2005]. Inside of about 15 R_S, there is a depression in the residual magnetic field. The slowly varying negative perturbation of the averaged dB_θ near periapsis can be accounted for by a symmetric ring current. An 11 h running average of dB_θ is plotted in the same panel with a red line. The sinusoidal oscillation with a period near that of the SKR superposed on the ring current signature gives evidence of a rotating asymmetric ring current [*Krimigis et al*., 2007; *Khurana et al*., 2009; *Provan et al*., 2009b; *Brandt et al*., 2010]. This feature is seen clearly in the blue line, a 4 h running average of dB_θ. We define the difference between the 11 h running average and the 4 h running average, i.e., the sinusoidal perturbation associated with the asymmetric ring current, as δB_θ, and plot it in Figure 1 (bottom).

Inside of 15 R_S, the magnetic field can be well approximated by the SOI model plus perturbations due to the symmetric and asymmetric ring currents: $\mathbf{B} = \mathbf{B}_{\mathrm{SOI}} + \mathbf{dB} + \boldsymbol{\delta}\mathbf{B}$; $|\boldsymbol{\delta}\mathbf{B}| \leq |\mathbf{dB}| \leq |\mathbf{B}_{\mathrm{SOI}}|$. The periodic variation of $\boldsymbol{\delta}\mathbf{B}$ has been examined extensively by *Andrews et al*. [2008, 2010a, 2010b] and *Provan et al*. [2009a, 2009b]. In comparing with plasma bulk properties, we focus on rotation phase-dependent variations of magnetic pressure, which, to lowest order in the near-equatorial regions, depend on δB_θ as

$$\delta P_{\mathrm{mag}} \approx B_\theta \cdot \delta B_\theta / \mu_o \tag{1}$$

Magnetic pressure perturbations associated with the asymmetric ring current were calculated for every measurement in our data set.

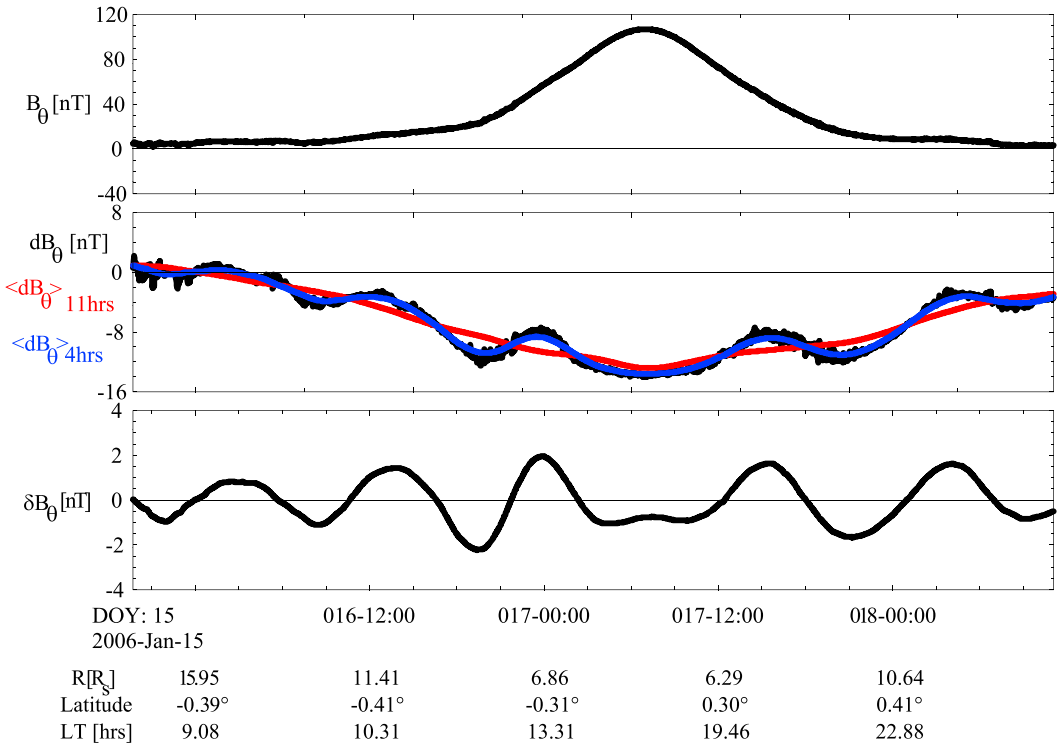

Figure 1. The magnetic field data in nanotesla versus UT (day of year and hour) from a typical periapsis pass by Cassini from 15 January 2006 to 19 January 2006. (top) The θ component of the magnetic field (B_θ) in spherical polar. (middle) The black line is the residual of B_θ, defined as the difference between the measured B_θ and the field of the Cassini SOI dipole [*Dougherty et al.*, 2005]; the red line is an 11 h running average of the residual, labeled $\langle dB_\theta \rangle_{11\text{hrs}}$; the blue line is a 4 h running average of the B_θ residual, or $\langle dB_\theta \rangle_{4\text{hrs}}$. (bottom) The curve is the difference between the red line and the blue line, δB_θ.

2.4. Nonuniform Distribution of Plasma Data

In establishing the rotation phase-dependent variations of ion bulk parameters, we are constrained by nonuniform data coverage of which it is important to be aware. On many of the orbits used in this study, Cassini traversed similar spatial paths (radial distance versus LT) through Saturn's magnetosphere. Coincidentally, the spacecraft repeatedly returned to the same radial position at almost the same SLS4S phase. In Figure 2, we show where (a) magnetic field and (b) plasma data were acquired in plots of local time versus radial distance. Each point is colored by local time-corrected SLS4-S phase (rotation phase). It is clear that large regions of local time are poorly covered in the data set, especially near dawn and dusk. In addition, the aliasing in radius by rotation phase is easy to see, as the colors at the same radial distance repeat multiple times. For example, predominantly cyan and orange/blue curves indicate that almost all of the data at 6 R_S were acquired at phases between 120° and 240°. At 8 R_S, all of the data were acquired at phases less than 120° and greater than 240°.

Strong coupling between rotation phase and radius can produce misleading results when data that vary strongly in radius are plotted versus phase. Figure 3 reveals that both the (a) ion density and (b) plasma pressure vary strongly (close to exponentially) with radial distance over the range of interest, and so we remove the phase-averaged radial trend before investigating the variation of pressure with rotation phase. The phase-dependent aspects of radial gradients (if any) remain in the data. We obtain the radial trends by fitting second-order exponentials to the data and have plotted the fits over the data in Figures 3a and 3b. Figures 3c and 3d are plots of the differences between the data and the fits to their radial dependence for density and pressure, respectively. The ratios d*n*/*n* and d*P*/*P* change little with radial distance: the amplitude of the perturbations is roughly 10% of the background. In section 3, we analyze the rotation phase dependence of these detrended perturbations.

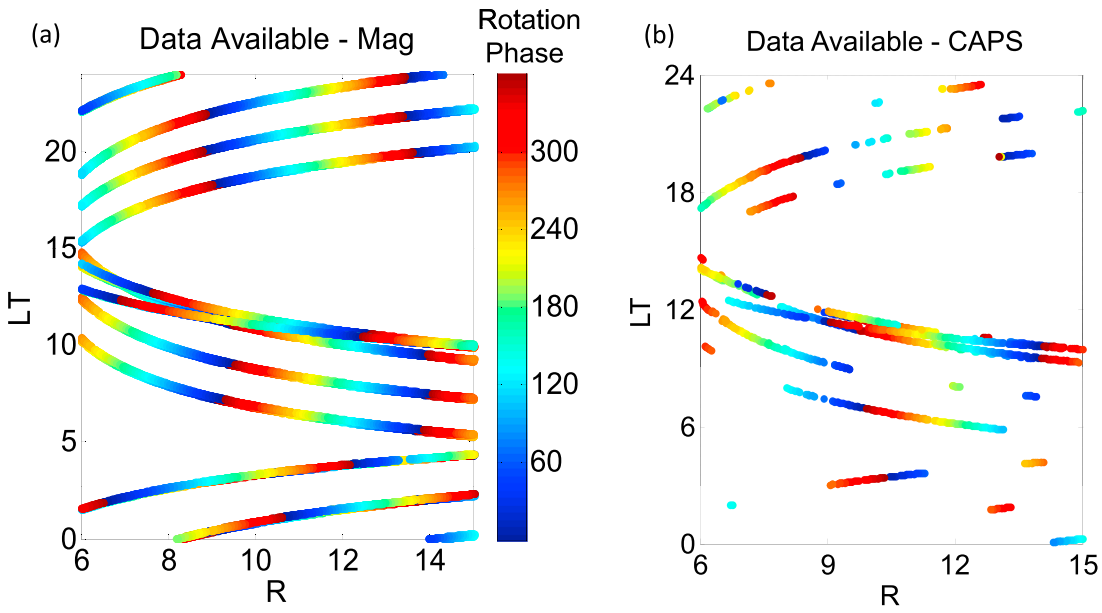

Figure 2. Plots of LT (hours) versus radius (R_S) of the positions of all available (a) MAG data and (b) CAPS data. Points are colored by rotation phase, i.e., the SLS4-S phase (degrees) corrected for the LT of the measurement.

2.5. North-South Displacements of Current Sheet: Effects on Plasma Properties Inside of 15 R_S

A number of factors cause the current sheet to lie above the planetary equator during the interval used in this study, so we must justify the use of measurements acquired slightly off the magnetic equator to represent equatorial measurements. The planet's spin axis is aligned with its magnetic dipole axis, but the magnetic equivalent dipole is offset 0.04 R_S northward of the center of mass of Saturn [*Smith et al.*, 1980]. Furthermore, during southern summer, Saturn's axis of rotation is inclined to its orbital plane so that the solar wind velocity has a finite northward component, and as a result its current sheet is bowl shaped [*Arridge et al.*, 2008], lying northward of the magnetic equator at a height that increases with radial distance over the radial range of interest. Additional displacement of the equatorial plasma sheet may result from periodic flapping of the tail current sheet. (During the interval of this study, the magnetic equator moved up and back periodically but rarely moved below the planetary equator [*Khurana et al.*, 2009].) We will show next that the plasma parameters inside of 15 R_S are little modified by these small north-south displacements of the magnetic equator, implying that the measured values are effectively equatorial values.

Plasma parameters near the equator have been shown to change slowly with north-south displacement from the magnetic equator. *Thomsen et al.* [2010] [see *Persoon et al.*, 2006] have used the form

$$n = n_o e^{-\frac{z^2}{3H^2}\left(1-\cos^6\left(\frac{z}{L}\right)\right)} \tag{2}$$

to organize the dependence of the plasma density (n) on distance along a dipole field line. Here z is parallel to the spin axis, L is radial distance to the equatorial point on the field line, and H is the scale height along a dipole field line, a function of radial distance. All are measured in R_S. Our data were acquired along parts of the Cassini orbit within 0.5° of the equatorial plane, or, equivalently, at $|z| \lesssim 0.13$ at 15 R_S, the outermost limit of our study. The density-scale height, H, for the dominant water group ions at the centers of the radial bins that we will examine is ~3 R_S at 13.5 R_S, 2.2 R_S at 10.5 R_S, and 1.5 R_S at 7.5 R_S [*Thomsen et al.*, 2010], increasing to 3.5 R_S at 15 R_S. Energetic particle-scale heights such as those investigated farther down the tail by *Sergis et al.* [2011] and *Arridge et al.* [2011] are expected to be larger. We use the simulation of *Jia et al.* [2012] (described in section 2.7.1 below) to establish that flapping leads to a maximum displacement of the current sheet of 0.8 R_S at 13.5 R_S, the center of the outermost bin. The northward displacements (dipole offset, bowl-shaped distortion, northward flapping), if acting concurrently at a time when Cassini was at the lowest latitude used in our data set, would imply that the measurements could have been as far as 1 R_S from the center of the current sheet at 13.5 R_S, which would change the plasma density by no more than 10%, a change that is

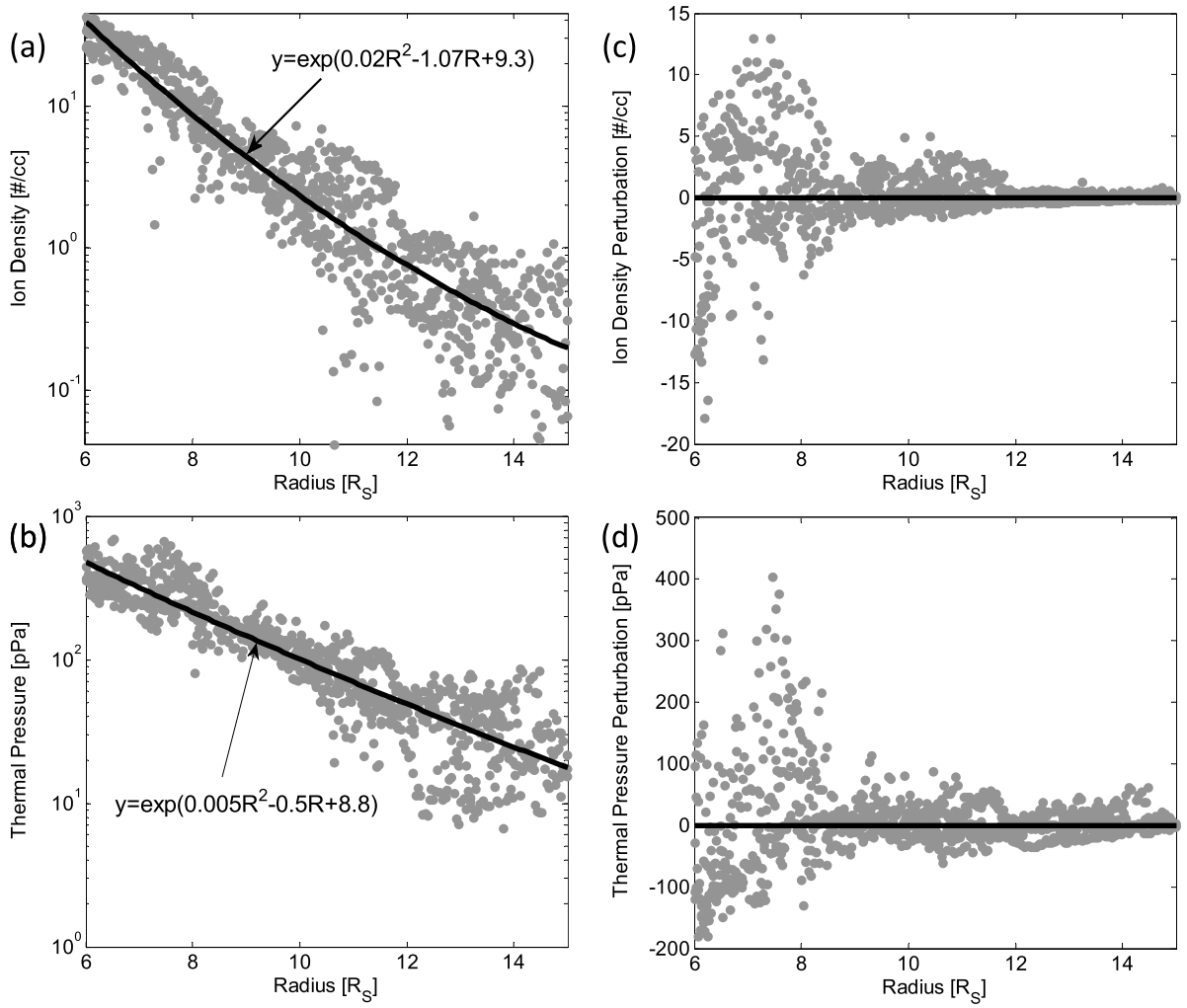

Figure 3. (a) CAPS ion number density (#-cm^{-3}) and (b) CAPS + MIMI total plasma pressure (pPa) versus radius (R_S) from 11 October 2005 to 24 May 2006 versus radial distance between 6 and 15 R_S. The black lines represent second-order exponential least squares fits with the equations displayed in the figures. (c) The CAPS ion number density and (d) CAPS + MIMI total plasma pressure with the radial trends removed by subtracting the fits on the left from the data.

small compared with the changes that we will show are organized by rotation phase. Hence, we do not correct the plasma data for distance from the current sheet and we use near-equatorial measurements as representative of values at the magnetic equator. The temperature of the plasma changes little with small displacement from the center of the plasma sheet, so the analysis can also be applied to the change of thermal pressure.

2.6. Radial Binning

Low-energy ions account for most of the plasma density in the magnetosphere. Pressure is provided by both dense, low-energy ions and tenuous, high-energy ions, but the contribution of ions of different energies to the total pressure varies with distance. *Sergis et al.* [2010] found that in the equatorial ring current between 6 and 9 R_S, the thermal ion plasma is the major source of particle pressure. The contribution of the energetic particles to the pressure becomes comparable to that of the thermal ions outside of 9 R_S and becomes dominant beyond 12 R_S. Sergis et al. report that the inertial body force and the radial pressure gradient force are comparable at 9–10 R_S, with the pressure gradient contributions becoming dominant outside of 11 R_S. We define our radial bins following the changing characteristics of the plasma environment, separating the data by radial cuts from 6 to 9 R_S, where thermal ion pressure dominates the energetic particle pressure and magnetic pressure; 9 to 12 R_S, the center of the ring current, where the ion plasma pressure and energetic particle pressure are nearly equal; and 12 to 15 R_S, where energetic particle pressure dominates the cold ion plasma. It

is worth noting that even in regions where the energetic particles dominate the pressure, they contribute to density and average drift velocity at most at the few percent level.

2.7. Local Time Binning

Local time asymmetries of magnetospheric properties are known to be significant. Day-night asymmetries have been observed in moon microsignatures [*Roussos et al*., 2005; *Paranicas et al*., 2005a], charged-particle drift paths [*Paranicas et al*., 2010], plasma flow [*Wilson et al*., 2013], and plasma temperature and energy flux [*Thomsen et al*., 2012] in Saturn's inner and middle magnetosphere. Furthermore, simulations by *Jia et al*. [2012] and *Kivelson and Jia* [2014] show periodic magnetopause displacements of ~5 R_S associated with large-scale expansions and contractions of the dayside magnetosphere that produce different effects at different LTs. For these reasons, it would be desirable to investigate the possibility of LT effects on the form of the perturbations. However, the limited data preclude analysis in multiple LT bins. We investigate whether the waveforms are likely to vary greatly with LT by examining the local time variations of plasma responses in a magnetohydrodynamic (MHD) simulation.

2.7.1. MHD Simulation

In order to understand how periodic behavior is imposed on Saturn's magnetosphere, *Jia et al*. [2012] developed a magnetohydrodynamic simulation in which they impose vortical flow perturbations along the equipotentials of one cycle of the $m = 1$, fifteenth spherical harmonic in the ionosphere centered at 70° latitude (dipole $L = 8.5$) in the southern hemisphere. The vortical flows, which extend from ~64° (dipole $L = 5.5$) to ~76° (dipole $L = 15$) in latitude, drive a pattern of field-aligned currents into the magnetosphere and the northern ionosphere. The imposed currents (that vary sinusoidally) rotate about the spin axis with a period of 10.8 h. Although it has been disputed whether the field-aligned currents are driven from the ionosphere or arise from processes elsewhere in the magnetosphere, there is no reason to question that at Saturn there is a system of field-aligned currents rotating at the SKR period and a quantitative model of the global response to a rotating current system helps us interpret the plasma periodicities observed. We have extracted information on the periodic responses of plasma parameters at different local times and radial distances.

In the simulation, the properties of the solar wind are held constant, so magnetospheric dynamics are driven by internal processes. The vortical flows in the equatorial plane of the magnetosphere are opposite in direction to what *Andrews et al*. [2008] refer to as the core field inside the cam region. These flows are analogous to the magnetospheric vortices identified by *Gurnett et al*. [2007]. The simulation was allowed to run for 100 h without the vortical flows to obtain the baseline magnetosphere. Then, the flow vortices were turned on and the simulation ran for another 50 h to allow the magnetosphere to stabilize. All results we show will feature time steps taken later than 150 h of simulation time.

Figure 4a illustrates streamlines of the flow imposed in the southern ionosphere at an arbitrary time step in the simulation, and Figure 4b shows schematically the corresponding pattern of flow in the equatorial plane of the magnetosphere. These patterns rotate at a prescribed rate as implied by the green arrows in the figures. The dotted circles in Figure 4b are 5 R_S apart. Equatorward flow perturbations in the ionosphere correspond to radially inward flow perturbations in the magnetosphere. Conversely, poleward flow perturbations correspond to radially outward flow perturbations in the magnetosphere. In this schematic, we would expect the pressure to increase between 5 and 10 R_S at the bottom of Figure 4b where the flows are converging and to increase in the same radial range at the top, where flows are diverging. This system of high- and low-pressure perturbations separated by 180° would rotate about the planet. The semirigid rotation of magnetic field fluctuations about Saturn has been well studied [*Andrews et al*., 2010b] and, as previously noted, magnetic pressure = $B\delta B_\theta/\mu_o$ varies with rotation phase in the same way as does δB_θ. The simulation shows that a localized source of compressional waves at low altitudes develops near the ~70° invariant latitude flux tube [*Kivelson and Jia*, 2014]. These compressional waves make their way relatively slowly (~6 R_S/h) through the equatorial regions of the large magnetosphere and decay in amplitude as they move away from their source, imposing perturbations throughout the middle magnetosphere. The fundamental wave speeds vary greatly over the simulation domain. In the equatorial region the Alfvén speed varies from about 400 km/s inside of 10 R_S to <35 km/s beyond 10 R_S (minimum values of about 12 km/s in the 20–23 LT sector). Near the equator, the sound speed is less than 60 km/s inside of ~8 R_S and rises to near 100 km/s beyond ~8 R_S and inside of ~15 R_S. Propagation of fast perturbations along the background field occurs at much higher

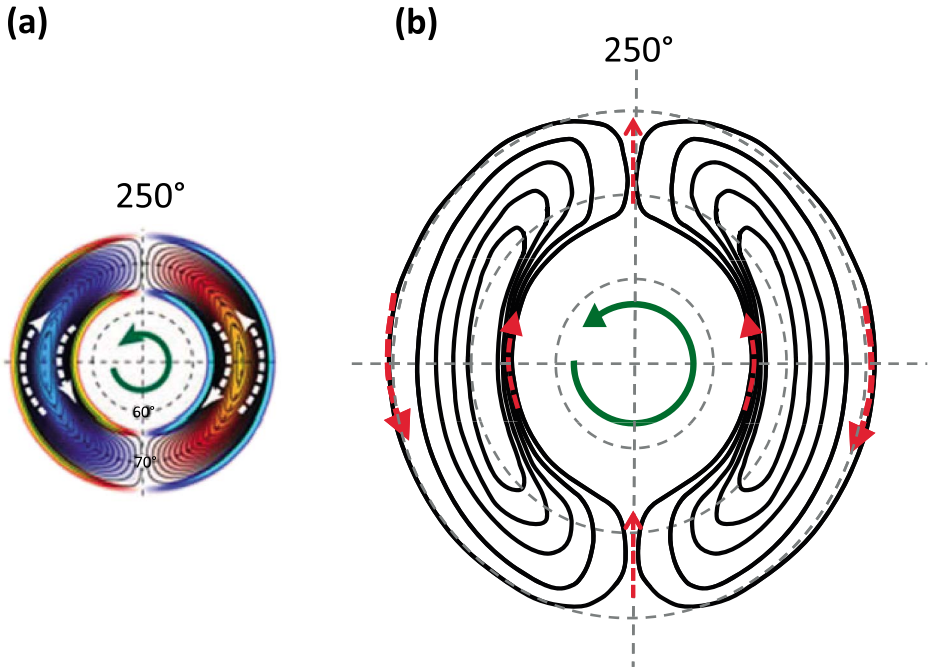

Figure 4. Schematics showing the assumed flows in the simulation of *Jia et al*. [2012]. (a) The vorticity imposed in the southern ionosphere in the *Jia et al*. [2012] simulation at an arbitrary step of the simulation. The vortices, which vary sinusoidally in azimuth, are centered at 70° latitude (dipole $L = 8.5$) and extend in latitude from ~64° to ~76° (dipole $L = 5.2$ to 17). The colors represent vorticity parallel to the local magnetic field, while the dotted white arrows show the direction of flow in the ionosphere. The green arrow indicates that the entire pattern rotates at the period of southern SKR. (b) A sketch showing schematically the flows in the magnetosphere imposed by flows in the ionosphere. Red arrows denote the direction of flow along the black lines. Dotted gray circles mark 5 R_S increments. As in Figure 4a, the green arrow indicates rotation of the pattern. The SLS2-S phase (left handed) toward which the core field points is indicated in both images as per *Andrews et al*. [2010b].

speeds. In the range of L shells that we analyze, near the equator the speed is about 400 km/s and increases to 5000 km/s at high latitudes within a few R_S of the ionosphere.

As described in *Kivelson and Jia* [2014], the simulation reproduces the magnitude and variation of the periodic displacement of the magnetopause, an element of what we refer to as breathing, better than it represents the phases at which the excursions occur. The phase delay is interpreted by noting that the MHD simulation [*Jia et al*., 2012] does not incorporate the contributions of energetic particles and, correspondingly, the sound speed is underestimated outside of ~9 R_S [*Kivelson and Jia*, 2014] where the thermal pressure of energetic particles becomes of the order of that of the bulk plasma [*Sergis et al*., 2010]. Near 15 R_S, the energetic particle pressure is ~3/2 the pressure of the thermal particles. Wave speeds are proportional to the square root of the pressure, so the wave speed in the simulation is roughly 0.6 of the actual value in the outermost bin (12–15 R_S) that we analyze. Fast mode waves, therefore, propagate too slowly outside of ~9 R_S in the simulation, leading us to expect an offset in the peak phase of pressure perturbations between the simulation and the data.

One might ask whether the mean flow speed is also underestimated in a simulation that does not include the effects of energetic ions, which drift more rapidly than thermal particles. Our calculations show that at 10.5 R_S, energetic particles (50 keV), which make up only 3% of the plasma density in the middle radial bin, drift relative to the thermal plasma at about 12.5 km/s and thus modify the bulk background of 70 km/s by only ~1%. Therefore, energetic particles do not shift the phases of the periodic perturbations of plasma parameters significantly.

The simulation has been found to reproduce quantitative elements of perturbations in Saturn's magnetosphere, including the periodic motions of the magnetopause [*Clarke et al*., 2010a, 2010b; *Kivelson and Jia*, 2014; *Pilkington et al*., 2015], the flapping and phase-dependent variations in thickness of the magnetotail

current sheet [*Khurana et al*., 2009; *Arridge et al*., 2011; *Provan et al*., 2011, 2012; *Jia and Kivelson*, 2012], variations of electron plasma density in the inner magnetosphere [*Gurnett et al*., 2007; *Jia et al*., 2012], and the noon-midnight electric field [*Thomsen et al*., 2012; *Jia and Kivelson*, 2016]. We expect it to give meaningful insight into the properties of the periodic plasma responses, possibly with some delays in phase in the outer part of the region that we investigate. The amplitude of the oscillations may be reduced somewhat because of insufficiently small grid scales and/or more dissipation than in the real system.

We first consider the patterns of simulated plasma and field perturbations in the equatorial magnetosphere through a rotation period. Figure 5 shows plots of selected plasma and field properties in the equatorial plane of the simulation at time steps separated by 3 h starting at 195 h. The pink dots on the axes mark 5 R_S intervals. The green dots are magnetic field lines mapped to the equatorial plane from 70° latitude in the ionosphere at locations separated by 15° in longitude. Noon is toward the left, and the location of the dayside magnetopause is marked with an orange line. The columns, from left to right, show density perturbations, plasma pressure perturbations, magnetic pressure perturbations, and total pressure perturbations: the sum of the magnetic and plasma pressures. Perturbations were extracted from the simulation by removing the average of the previous five 10.8 h cycles for each pixel. The black arrows (unit vectors) show the orientation of magnetic field perturbations in the equatorial plane. It is readily apparent that the magnetic pressure perturbations inside of ~12 R_S rotate almost rigidly, as described by *Andrews et al*. [2008] and *Provan et al*. [2009b], corresponding to a very structured variation with rotation phase, but the other quantities plotted do not. Beyond ~12 R_S none of the plotted quantities rotate without significant change in structure.

2.7.2. Defining LT Bins

In order to examine how various properties of interest vary with rotation phase at different radial distances and local times, we select points in the simulation corresponding to the centers of the radial bins used to analyze the data (e.g., for the 6–9 R_S bin, we sample at 7.5 R_S) every 3 h of LT and plot the dependence of the perturbations on rotation phase. In Figure 6, we show how the magnetic pressure, ion density, and plasma pressure perturbations at different radial distances and different LTs vary with rotation phase in the simulation. To the upper right of the figure is a "clock" with hands whose colors identify the LTs at which the similarly colored curves in the other columns were extracted. It is evident from Figure 6 that the peak phase and shape of the waveforms extracted from the model are nonsinusoidal and change with local time. Where the forms of the simulated variations are similar over a range of LT, we assume that it is meaningful to group measured values of the corresponding properties over that range of LT and thereby improve the poor statistics in the data.

In the case of magnetic pressure perturbations in the 6–9 R_S range, the waveforms vary little with LT (roughly the same amplitude and peak phase), other than near noon (magenta curves) where the waveform is considerably different than at other LTs, possibly due to the motion of the magnetopause. From 9–12 and 12–15 R_S, the LT bins from 12 to 21 LT display two peaks: one that coincides with the peak in the dawnside bins and a second one that occurs later.

Our data set, however, lacks the coverage needed to examine the predicted local time dependence of the magnetic field perturbations. In Table 1, we show how many magnetic pressure data points were available within each LT and radial bin. There are few measurements in the postnoon sector in any radial bin. Therefore, it is not appropriate to separate the measurements into local time bins.

Like the magnetic pressure, the variation with rotation phase of the simulated ion density between 9 and 15 R_S changes little with LT, so there is no need to divide the measurements into separate LT bins. However, the density perturbations from 6 to 9 R_S differ significantly in different LT bins. On most of the dayside (from 1030 to 1930 LT), the waveform peaks near 70° rotation phase, but on the nightside (1930 to 0730 LT) it peaks near 120°. The phase of the dayside peak corresponds closely to the phase of a local minimum in the nightside density variation. The waveform in the bin centered at 9 LT differs markedly from both of the structures identified in the innermost bin.

Insight from the simulation suggests that we should divide the 6–9 R_S bin into three local time bins: one from 1030 to 1930 LT, one from 1930 to 0430 LT, and one from 0730 to 1030 LT. However, there are no data in the bin centered at 0900 LT and few data in the 0730–1030 LT bin. The only LT bin with sufficient coverage in phase to analyze meaningfully is from late morning to past dusk (1030–1930 LT).

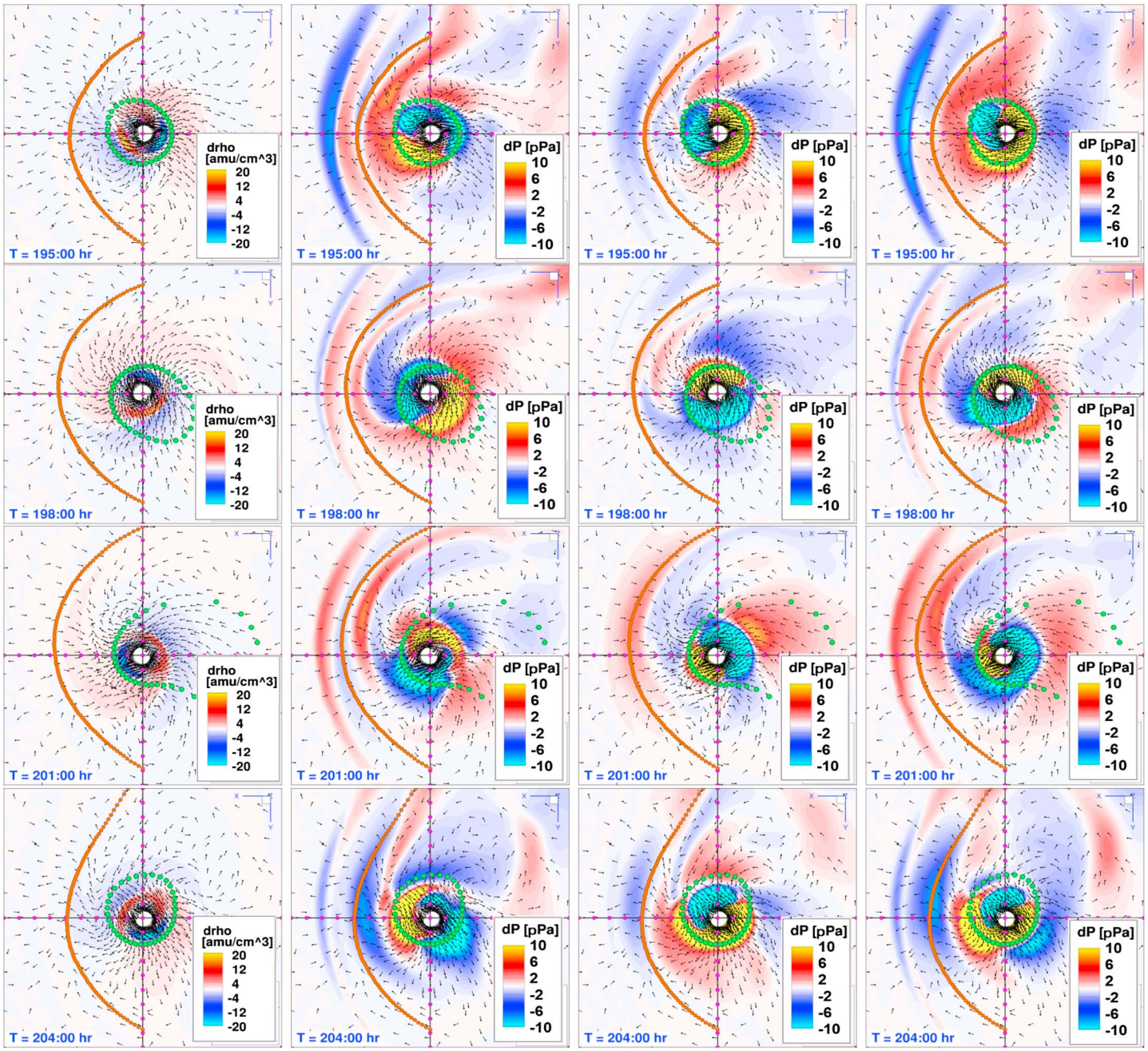

Figure 5. Snapshots of plasma and field properties in the equatorial plane from the simulation by *Jia et al*. [2012]. The snapshots are extracted every 3 h, starting at $t = 195$ h. The Sun is to the left, and the orange curve follows the location of the dayside magnetopause. The background colors represent (first column) ion density perturbations, (second column) plasma pressure perturbations, (third column) magnetic pressure perturbations, and (fourth column) total pressure perturbations. The green dots mark the intersection with the equatorial plane of field lines emerging from latitude 70°S and separated azimuthally by 15°.

The peaks of the simulated plasma pressure waveforms from 6–9 and 9–12 R_S in Figure 6 (third column) are fairly close in phase at all LTs, but the troughs are long and drawn out, with absolute minima falling between 120° and 240°, depending on the LT. Again, however, the distribution of the data favors the dayside (see Table 2, which shows the distribution of plasma data in radial distance and local time), so dividing the data into different LT bins would not be meaningful. In the outermost range of our analysis (12–15 R_S), the waveforms of the plasma pressure perturbations versus rotation phase vary dramatically with LT. On the duskside (orange, gray, and gold) there is a clear minimum near 240°, while on the dawnside (green and red) there is a clear minimum near 70°. There is an almost 180° shift in peak phase between the premidnight and

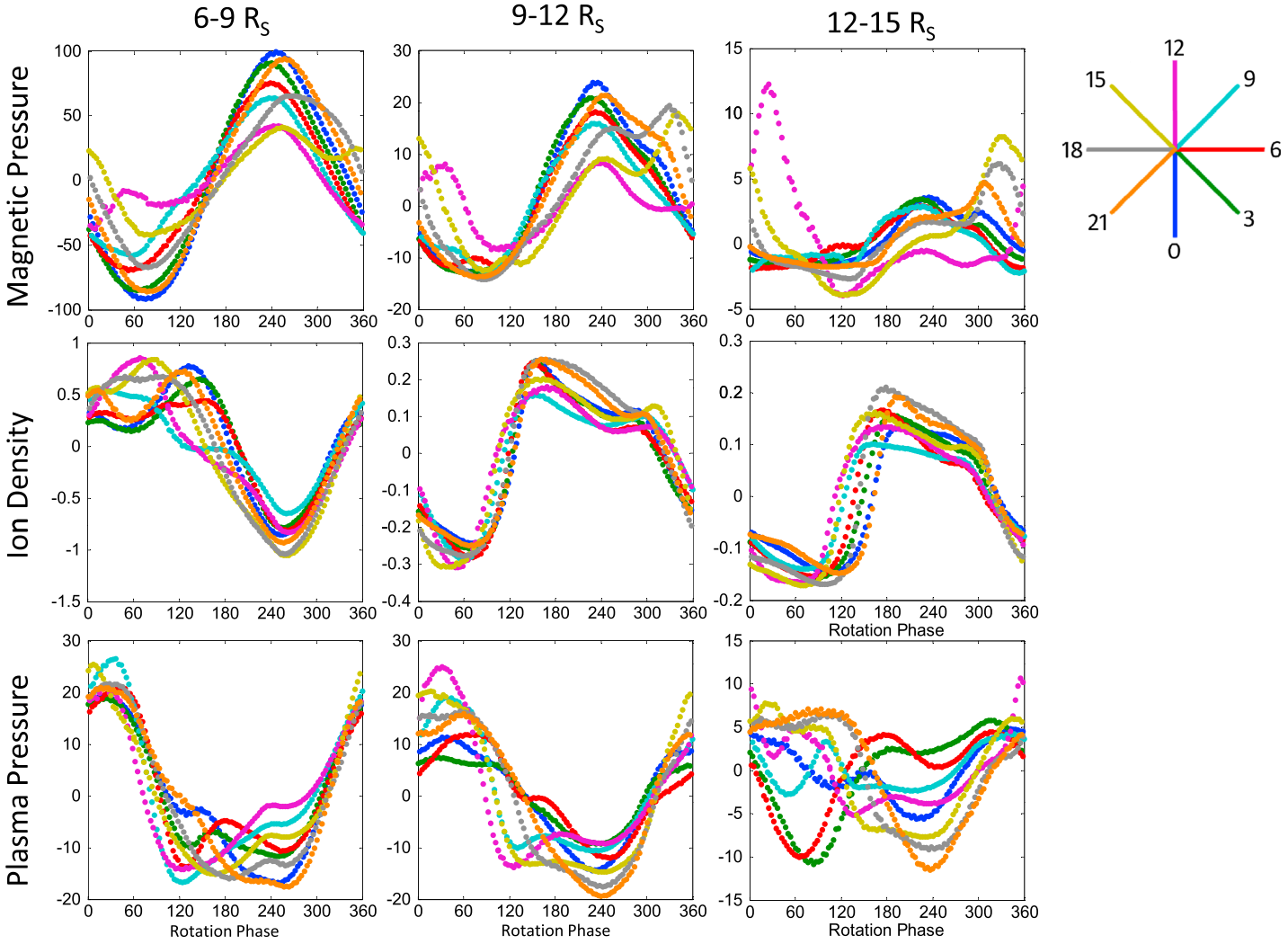

Figure 6. Local time variation of field and plasma perturbations in the equatorial plane from the simulation. (first row) The magnetic pressure perturbation (pPa) over one full cycle sampled every 3 h in local time at radial distances of (first column) 7.5 R_S, (second column) 10.5 R_S, and (third column) 13.5 R_S. The colors of the curves identify the LT to which they apply and correspond to the colors in the clock figure on the right. (second row) As in Figure 6 (first row) but shows ion density perturbations (#-cm^{-3}). (third row) The plasma pressure variations (pPa).

postmidnight LT sectors. Guided by these findings, we divide our observations in the outermost radial range into two separate LT bins, one combining the bins centered at 0300 and 0600 LT and covering the LT range from 0130 to 0730 LT and one combining the bins centered at 1500, 1800, and 2100 and extending from 1330 to 2330 LT. After the data were divided into local time and radial bins, the points in each bin were plotted versus SLS4S phase. The results are shown in Figure 7 and discussed below.

Table 1. Radial and LT Distribution of Magnetic Measurements Used in This Study[a]

	6–9 R_S	9–12 R_S	12–15 R_S
0 LT	1114	1801	947
3 LT	668	883	2248
6 LT	89	900	1287
9 LT	1455	1255	3459
12 LT	2989	2607	338
15 LT	873	0	0
18 LT	1621	892	25
21 LT	1356	1180	1861

[a]Entries indicate the number of measurements within each 3 h LT bin centered at the LT specified in the first column.

3. Results

After processing the data as described in section 2, we plotted the measured values of magnetic pressure, ion density, and ion pressure perturbations versus rotation phase in designated radial bins over two complete cycles

Table 2. Radial and LT Distribution of Plasma Measurements Used in This Study[a]

	6–9 R_S	9–12 R_S	12–15 R_S
0 LT	12	8	29
3 LT	2	37	22
6 LT	0	57	23
9 LT	45	52	170
12 LT	105	164	4
15 LT	28	0	0
18 LT	79	21	0
21 LT	19	19	31

[a]Entries indicate the number of measurements within each 3 h LT bin centered at the LT specified in the first column.

(Figure 7). Each row contains the data from all LT unless otherwise indicated. For each parameter in each bin, the data are grouped into 10 rotation phase bins with equal numbers of points, except for the plasma pressure in the outermost bin where we use only seven rotation phase bins due to a paucity of points. The red circles are the medians of both the analyzed parameter and its phase in each phase bin. The error bars extend ± 1 standard error of the mean. A sinusoidal fit to the medians was performed, and the result is plotted on each graph in black.

In order to determine the goodness of fit, we calculate the coefficient of determination, or $R^2 \equiv 1 - \mathrm{SS_{res}}/\mathrm{SS_{tot}}$, which indicates how well the total variation of the bin medians are explained by the fit, with 1.0 meaning that there is perfect correlation between the data and the fit and 0 meaning that there is no correlation. Here $\mathrm{SS_{res}}$ is the sum of squares of the residuals, and $\mathrm{SS_{tot}}$ is the total sum of squares of the data values. The values of R^2, as well as the number of points in each radial bin, are noted on the graphs, and the peak phases and amplitudes of the sinusoidal fits are noted in the titles of the graphs.

We find that magnetic pressure oscillations are well organized by SLS4S phase with peak at phases between 254° and 284°, increasing from 6 to 15 R_S. Perturbations in the magnetic pressure, $P_{\mathrm{mag}} = B \cdot \delta B_\theta / \mu_0$, result from periodic variations of δB_θ whose behavior inside of 15 R_S has been analyzed previously [*Andrews et al*., 2008, 2010b; *Provan et al*., 2009b, 2011]. *Andrews et al*. [2010b], using data from a longer time interval than that used in this study and taken within 5° of the dipole equator, established that δB_θ peaks at $250 \pm 20°$ rotation phase between 6 and 9 R_S and that the peak shifts by order of 30° out to 15 R_S. The peak phase in our analysis is within the error of the observed peaks in δB_θ in *Andrews et al*. [2010b] and in the simulation (Figure 6).

Despite the sparse measurements of plasma parameters, Figure 7 shows that there is a periodic variation of total plasma pressure and density with rotation phase. However, some anomalies require explanation. For example, although the observed peak of the magnetic signature shifts by only ~30° between the 6–9 R_S bin and the 12–15 R_S bin, the observed peak of the density perturbations shifts by 185° between the 6–9 R_S bin and the 12–15 R_S bin. The observed peak of the total pressure perturbations shifts by 176° across the midnight meridian in the 12–15 R_S radial bin, although the sinusoidal fits are admittedly poorly constrained and, in both cases, the minima are identified by a single median point.

The phase relationships among the parameters are also of interest and call for interpretation. In the 6 to 9 R_S bin, magnetic pressure perturbations are in lagging quadrature with the thermal pressure perturbations and leading quadrature with the ion density perturbations. Within the error of the fits, density perturbations are in antiphase with thermal pressure perturbations. In the 9 to 12 R_S bins, the magnetic pressure perturbations are in phase with the density and plasma pressure perturbations. In the 12 to 15 R_S bin, the magnetic pressure and density perturbations are in phase but the thermal pressure is again in quadrature; the magnetic pressure leads the thermal pressure on the dawnside and lags on the duskside. The challenge is to interpret these phase relations in terms of a superposition of the effects of the rotating field-aligned currents (FACs) and the expansion and contraction of large portions of the magnetosphere.

Kivelson and Jia [2014] have shown that the rotating field-aligned currents in the simulation launch waves that drive the large-scale compressions and expansions of the magnetosphere. A fast-mode compressional wave in a uniform system has magnetic pressure perturbations in phase with thermal pressure perturbations, but we find that the thermal and magnetic pressure perturbations are not everywhere in phase. *Kivelson and Jia* [2014], following *Southwood* [1977], point out that in a nonuniform system the fast and slow modes are coupled; centrifugal acceleration further complicates the relationships between perturbations of magnetic pressure and thermal pressure, and consequently the phase relations may differ from those expected for compressional waves propagating across the background field in a uniform, nonrotating system.

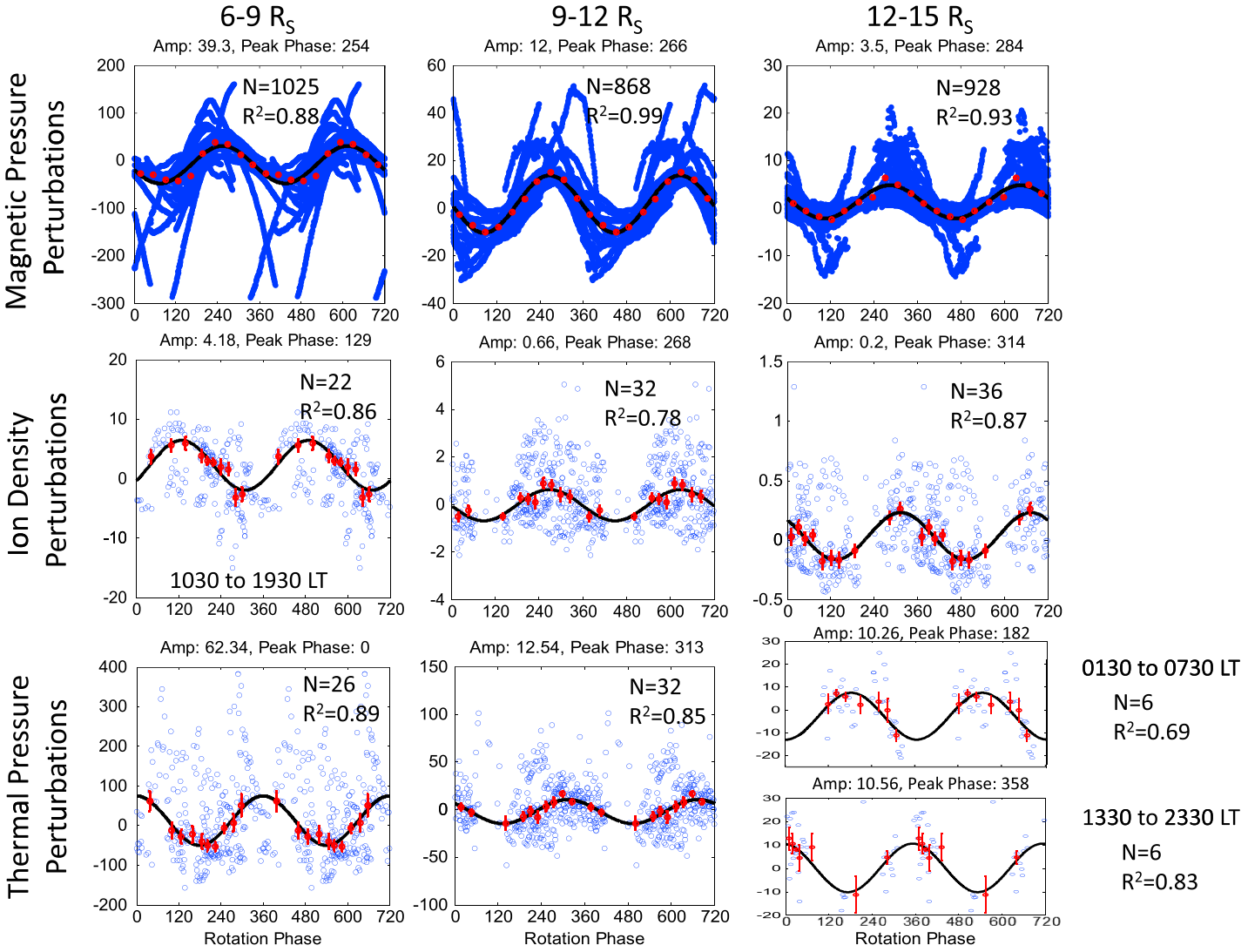

Figure 7. Field and plasma perturbations versus rotation phase in degrees over two cycles. (first row) The magnetic pressure perturbations (pPa). The results of the analysis of (second row) ion density perturbations (#-cm^{-3}) and (third row) plasma pressure perturbations (pPa). The results for radial bins from (first column) 6 to 9 R_S, (second column) 9 to 12 R_S, and (third column) 12 to 15 R_S. All plots include data (blue dots) from Cassini measurements at all LT unless otherwise noted. Red circles mark the median perturbations and phases in 10 bins with equal numbers of points, except for the plasma pressure between 12 and 15 R_S, which was split into seven7 bins in order to improve statistics. The red bars about the medians represent one standard error of the mean above and below the median. A sinusoid, offset by the mean of the medians, with amplitude and phase as free parameters, was fit to the medians and is plotted in black. Points were weighted inversely by the standard error of the mean in each bin. The amplitude and peak phase of each sinusoid is marked in the title of each graph.

Nonetheless, the total pressure perturbations develop and compressional waves propagate in outward spirals as seen in Figure 5 (fourth column).

4. Interpretation

We have noted that the periodic signals, especially their phase relations, reflect the response of the field and plasma to the perturbations directly driven by the imposed rotating FACs and to the global-scale variations driven by compressional waves launched near the source of the FACs. Magnetic pressure versus rotation phase takes a simple form in the simulation and appears to be dominated by currents driven directly from the source in the ionosphere. The field-aligned currents couple to perpendicular currents that drive vortical flow in the equatorial plane. The core field points toward the maximum in magnetic pressure perturbations (~250°) and rotates with a 10.8 h period. Inward of the FACs, the flow converges near ~250° rotation phase

(see Figure 4b), creating a maximum in magnetic pressure in the ~64–70° invariant latitude (λ) range (that maps roughly to our 6–12 R_E radial bins and slightly beyond), and diverges at higher invariant latitudes, where it reduces the magnetic pressure near ~250°. The magnetic pressure in the 6–9 and 9–12 R_S bins peaks close to the expected phase. Outside of 12 R_S, especially near noon (see Figure 6), the variation is not as well organized in rotation phase, possibly because of the expected transition from converging flow to diverging flow. Understanding the peak phases of the plasma parameters is more difficult, because the signals do not merely rotate. We turn to the simulation to gain insight into the jumps in phase found in the plasma data.

4.1. Responses to Compressional Waves

We have noted that the ionospheric vortices and associated flows serve as the source of large-scale pressure perturbations that propagate outward from low altitudes. For example, in Figure 5 (fourth column) at hour 198.00, one can follow the leading edge of the pressure minimum (blue) from near 1800 LT to 1200 LT and estimate the radial velocity as ~60 km/s. The compressional waves produce perturbations that do not merely rotate; they cause large portions of the magnetosphere to change shape and scale [*Jia and Kivelson*, 2012; *Kivelson and Jia*, 2014]. For example, the total pressure perturbations (magnetic + plasma) in Figure 5 show that the magnetopause (orange line) moves in and out as it responds to alternating fronts of high pressure and low pressure on the dayside. Similar fronts on the nightside stretch and relax the field lines tied to 70° invariant latitude (follow the green dots down one of the columns in Figure 5 and note how they move down the tail and back). These are aspects of what we have called breathing of the magnetosphere. We put forward the hypothesis that in each cycle, the system experiences spinning, breathing, and flapping perturbations (the latter not pertinent to the core magnetosphere), all at the same period but not locked in relative phase and argue that this produces anomalies in the phases of peak perturbations of plasma properties in critical LT sectors. At a fixed radial distance, signal maxima of parameters dominated by the spinning response (e.g., $\boldsymbol{\delta B}$ and magnetic pressure) fall at nearly the same rotation phase at all local times, typically with peaks and troughs roughly 180° apart; they seem to be relatively little affected by breathing. However, the periodic changes in the size and shape of the magnetosphere resulting from propagating compressional waves affect plasma parameters near the equator at different rotation phases in different parts of the magnetosphere. In the data, we have identified two significant jumps in the phase of the peak of the sinusoidal fits: the plasma pressure perturbations remain within 50° of 360° except on the dawnside of the 12 to 15 R_S bin where the peak phase is close to 180° and the phase of the peak in density perturbations changes by up to 139° across between the 6–9 R_S and the 9–12 R_S radial bins. These shifts are far larger than the phase delay of 12°/R_S that *Cowley et al*. [2006] have identified as a propagation delay in the quasi-dipolar magnetosphere. We will find that the simulation shows that global expansion and contraction of the magnetosphere, i.e., the breathing response, affects the rotation phase dependence of density and plasma pressure and explains these jumps.

4.2. Breathing and the Distortion of Magnetic Shells

Distortions of the magnetospheric size and shape in the simulation can be described quantitatively by characterizing the distortion of shells of fixed invariant latitude as a function of rotation phase. In Figure 8 we show the points of intersection with the equator of constant invariant latitude shells traced from the ionosphere every 2° of latitude from 65° to 72° every 2 h LT from 195 h to 205 h of simulation time, close to a full cycle. Colors represent the invariant latitudes, and points emerging from the same LT are connected with black lines. A heavy black radial line marks 250° rotation phase. Supporting information Movie S1, a movie available online, provides a dynamic version of this figure. In Figure 8, it is immediately apparent that the size and shape of the invariant latitude shells in the middle magnetosphere change radically over one full cycle (note, for example, the expansion of the 70° invariant latitude shell previously represented in Figure 5). At hour 196 with the subsolar SLS4-S phase near 120°, the invariant shells bulge slightly near dusk. As this bulge rotates into the nightside it is no longer confined by the magnetopause and expands down tail. The bulge continues to stretch and rotate. Near dawn, the shells of invariant latitude become very stretched. When the stretched field lines enter the prenoon sector, the shells suddenly relax to a more circular configuration, suggesting that a plasmoid has been released and the field lines have collapsed toward Saturn like a slingshot. The release of the plasmoid is responsible for the impulsive increase in density in the simulation near 100° rotation phase at 10.5 and 13.5 R_S, which we will discuss in more detail later. The pulse-like signature has been described previously in studies of the magnetic field by *Yates et al*. [2015].

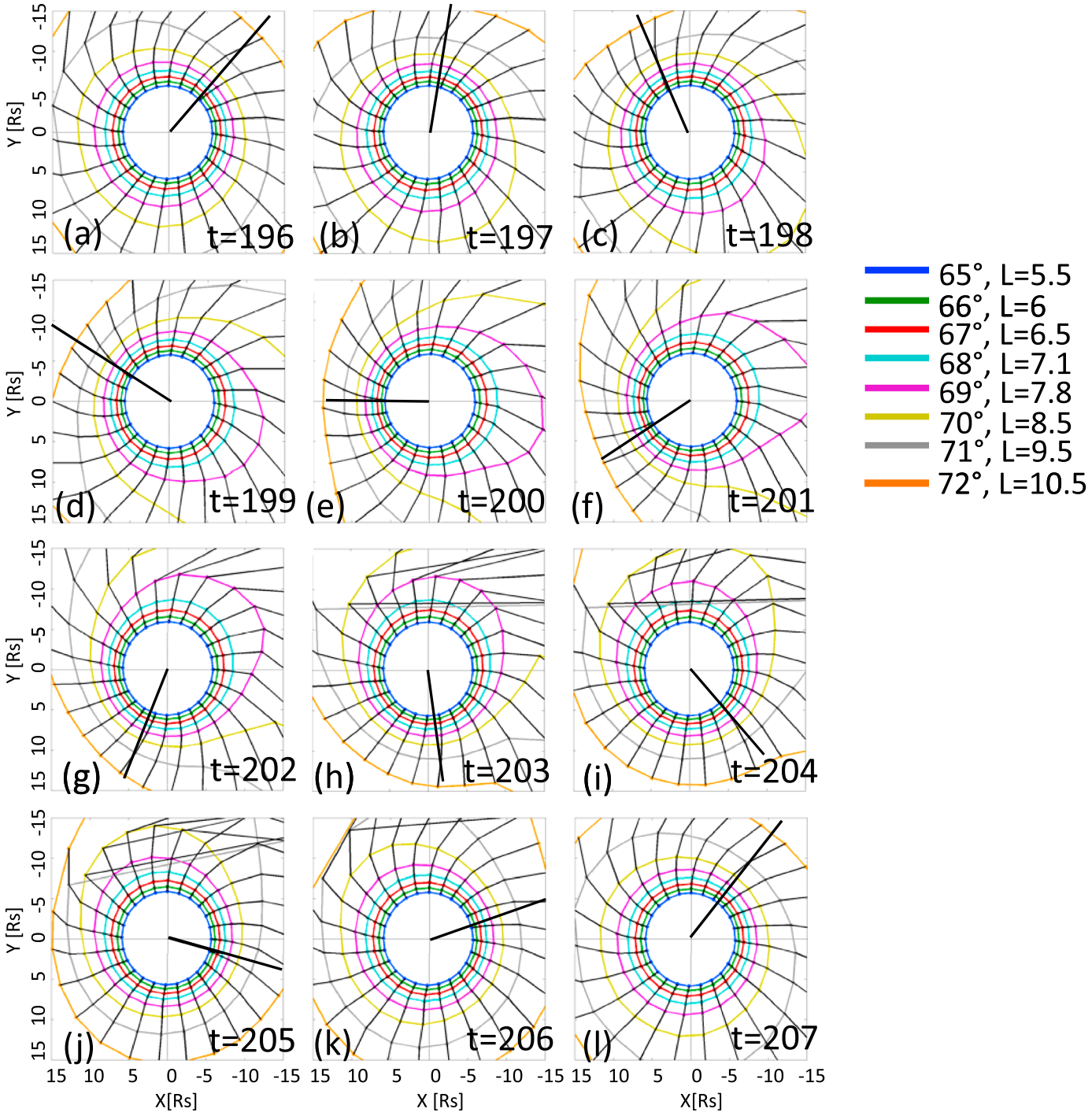

Figure 8. Changing size and shape of the middle magnetosphere. Colored dots mark the intersection with the equatorial plane inside of 15 R_S of field lines emerging from the southern ionosphere at every degree of latitude from 65° to 72° at increments of 15° in local time. Dots and lines of the same color emerge from a fixed latitude as indicated in the upper right, and black lines connect dots originating at the same local time. Noon is toward the left. The plots start at hour 195 and continue every 2 h over a full cycle. The heavy black radial line marks 250° rotation phase.

In the supporting information, Figure S1 expands the region shown in Figure 8 to reveal that the entire magnetosphere dramatically reconfigures itself once every cycle, changes that are reflected in the evolution of the middle magnetosphere described above. On the dayside, the magnetopause, whose location closely follows the location of the 80° invariant latitude shell over one cycle, moves in and out cyclically. In turn, the

dayside flux tubes in the middle magnetosphere (see Figure 8) compress and expand slightly. As plasma and magnetic flux tubes rotate around to dusk, at a critical rotation phase they begin to stretch rapidly down the tail. The plasmoid development is linked to the tangling of the outermost shell lines on the dawnside (see Figures S1 and 8h–8j) and is associated with the extreme outward displacement of the shells at highest invariant latitude. In Figure 8k, the outermost shells are less distorted, and in Figure 8l, the shells have become quasi-circular, much as in Figure 8a, as the dayside magnetosphere recovers from the plasmoid release. The effects of the plasmoid release cause the magnetopause to move farther outward on the dawnside than on the duskside [*Kivelson and Jia*, 2014]. The strong coupling between the rotating bulge and the expansion and contraction of the magnetosphere corresponds to what we refer to as breathing.

In order to understand more about the consequences of magnetospheric breathing, we must link its action in the equatorial plane to rotation phase. If a bulge in the magnetic shells were rotating at a constant rate, its effects would appear at a fixed rotation phase at every LT and would be indistinguishable from the effects of spinning or semirigid rotation. Figure 8 shows that this extreme situation does not apply. For instance, in Figure 8e, the bulge is located just before midnight at hour 200. At hour 201 (Figure 8f), the bulge has rotated azimuthally, but the maximum stretching is still centered at midnight. From hour 202 to hour 204, the bulge barely moves. This progression, in which the region of peak stretching rotates more slowly than SLS phase through the nightside of the magnetosphere, shows that spinning and breathing are not tightly coupled. On the dayside, the compressional wave creating the bulge (see spiral-shaped pressure fronts in Figure 5) rotates faster than the SLS4 phase, likely due to the collapse of the tail. Between hours 204 and 207, the bulge rotates through the LTs from dawn to dusk: at hour 204 the expanded region is located near dawn, and at 207 it is near dusk. Thus, the bulge has rotated through half a rotation in only a third of the 10.8 h period. Signals that rotate more slowly than the SLS4 phase will appear at decreasing SLS4 phase at increasing local time. Similarly, signals that rotate faster than SLS4 phase will appear at increasing SLS4 phase at increasing local time.

4.3. Breathing and Dayside Density

Scatter inherent in the data, arising from jitter [*Provan et al*., 2011], solar wind variability, and injection events, make it difficult to identify details of the signatures of periodic variations of the magnetosphere in the data plots, but, using global-scale information from the simulation, we can interpret variations with rotation phase of the simulated parameters. The analysis of the distortion of magnetic shells can be used to interpret the simulated density perturbations from 12 to 15 R_S in Figure 6 (second row). The simulated densities exhibit abrupt increases and slower decreases in slope at slightly different rotation phases in different LT bins. The density perturbations at 21 LT (orange) increase sharply near 126°. The sharp increase appears at decreasing rotation phase with increasing LT between 21 LT and noon: at midnight (blue) the sharp increase begins at about 120°, at 3 LT (green) the rise begins near 115°, at 6 LT (red) it is near 100°, and at 9 LT (cyan) it is near 90°. Correspondingly, in Figure 8 the magenta curve moves inside of 10 R_S at 21 LT at hour 202, at midnight at hour 203, at 0300 LT at hour 204, and at 0600 LT at 205, etc.; i.e., the compression advances faster than rotation phase. Correspondingly, in Figure 8 the bulge moves more slowly than the rotation phase from noon to dusk but the compression moves faster than rotation phase. This varying effect implies that the responses of the field and plasma are not tightly locked to SLS phase. The shifting phases of the key responses can be used to separate the effects of breathing from those of spinning.

Breathing is a global phenomenon that affects different parts of the magnetosphere differently. On the dayside, it is particularly evident in the in-and-out motion of the magnetopause, which is so closely linked to the expansion and contraction of the dayside magnetosphere that the magnetopause position can be used to characterize dayside expansion and contraction. Figure 9a shows the standoff distance of the noon magnetopause versus rotation phase from the simulation. Figures 9b–9d are the plots of density perturbations from the simulation for the different radial bins. We have marked the phases of the maximum and minimum magnetopause standoff distances with vertical lines on each graph. Given that the compressional waves on the dayside are propagating radially at about 70 km/s and that the typical outermost location of the magnetopause is near 28.5 R_S at noon at ~250°, one would expect that the peak of the compressional wave causing the outward displacement at noon at 13.5 R_S would have passed about 3.6 h earlier at a phase of ~250°–120° = 130° and that its trough (corresponding to minimum magnetopause displacement) would have passed 4.8 h earlier at ~290° rotation phase. We find no anomalies in

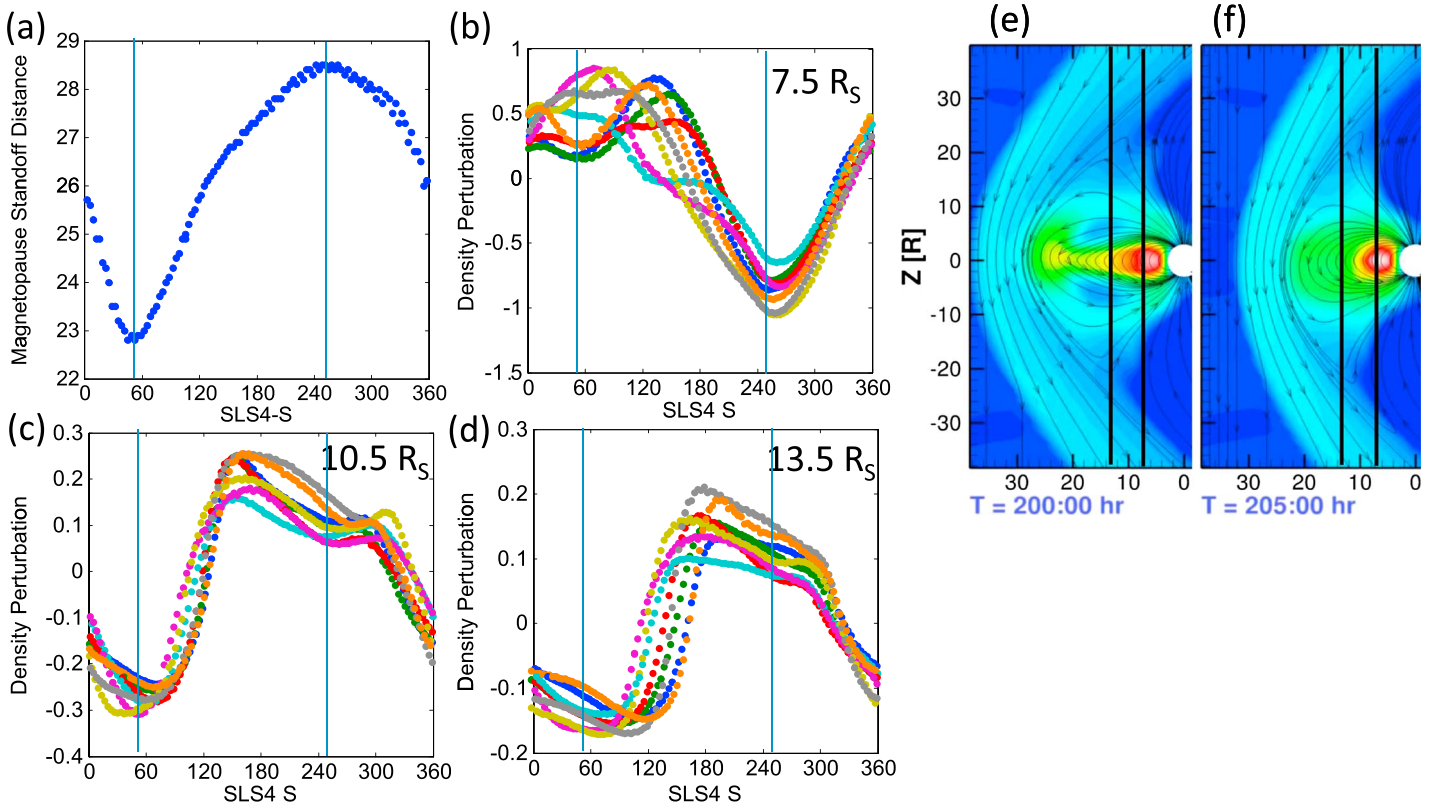

Figure 9. The effect of magnetopause motion in the simulation by *Jia et al.* [2012]. (a) The distance (R_S) of the nose of the magnetopause from Saturn over one cycle versus rotation phase (deg) at noon. The ion density perturbations (#-cm^{-3}) from the simulation at (b) 7.5 R_S, (c) 10.5 R_S, and (d) 13.5 R_S. Curves are colored by LT as in Figure 6. A noon-midnight meridian cut of the simulation (e) at hour 200, when the magnetopause is most expanded, and (f) at hour 205, when the magnetopause is most compressed. The background is colored by density perturbation, and 7.5 R_S and 13.5 R_S have been marked with black lines.

the magenta curve (plotted for noon) in Figure 9d at 130°, but there is a small but clear positive anomaly in the density near 290° phase. A similar bulge is seen at a slightly larger rotation phase in Figure 9c for the magenta curve representing noon 10.5 R_S. The compressional waves have little effect on density on flux tubes within the shells of the dominant FACs.

Having discussed expectations based on phase delays, it is initially puzzling to note that the maximum magnetopause standoff distance occurs at the same phase (~250°) as the minimum of the density oscillations in the 6–9 R_S radial bin (Figure 9b) at a phase when the density near noon in the 10.5 and 13.5 R_S bins is not far below its maximum value (Figures 9c and 9d, respectively). We can understand the large phase change in density across radial bins by examining Figures 9e and 9f, which are cuts showing the density in the noon-midnight meridian of the *Jia and Kivelson* [2012] simulation at the times at which the magnetopause is most expanded and most compressed. At $T = 200$ h, the magnetosphere is most expanded (see Figure 9e) and the SLS4 phase at noon is ~250°. Here the dayside field lines from 9 to 15 R_S are stretched and centrifugal forces have pushed plasma into the equatorial plane, creating an enhancement in plasma at the equator. Because centrifugal forces are not very important from 6 to 9 R_S, where rotation-related forces are relatively weak, there is no corresponding enhancement in the innermost bin and changes in plasma density result principally from the increased equatorial area of the flux tube associated with the development of a magnetodisk configuration [*Achilleos et al.*, 2010]. The reconfiguration due to the expanded dayside magnetosphere produces a trough in the density perturbation at 250° rotation phase at noon in the 6–9 R_S bin. Conversely, when the dayside magnetosphere is compressed at $T = 205$ h (see Figure 9f), there is a maximum in density perturbations in the 6 to 9 R_S bin and a minimum in the 9 to 15 R_S bins. The reconfiguration of the dayside magnetosphere associated with breathing is the dominant source of perturbations observed in ion density on the dayside.

4.4. Quantifying Breathing on the Nightside

The nightside perturbations in the regions inside of 15 R_S in the simulation can also be understood as partially controlled by magnetospheric breathing, i.e., the stretching and collapse of the magnetic flux tubes. In order to quantify the impact of breathing on the nightside magnetosphere, we must estimate the stretching of the flux tubes. The contribution of breathing to the rotation phase dependence of measurements varies with radial distance because the expansion and contraction of invariant latitude shells become increasingly significant in the outer magnetosphere on the nightside. Consequently, we concentrate on the region outside of 9 R_S, examining the periodic responses in the 9–12 R_S and 12–15 R_S bins in the simulation at premidnight (i.e., 21 LT), midnight, and postmidnight (3 LT). Using the simulation we have calculated $dr/d\lambda$, which we refer to as the stretching parameter, a proxy for stretching of flux tubes, at 10.5 and 13.5 R_S and the selected LTs over one phase cycle. Here dr is the radial distance at the equator between two invariant latitude shells (Figure 8) and $d\lambda$ is the difference of their invariant latitudes. We plot invariant latitude versus the dr values for each time step over a full cycle and fit the values with a spline fit.

To obtain the stretching parameter for each radial bin, we extract the slope of the spline fit ($dr/d\lambda$) at the invariant latitude corresponding to the desired radial distance. The stretching parameter is plotted versus rotation phase (blue dots) at radial distances of 10.5 R_S (Figure 10, first column) and 13.5 (Figure 11, first column). The dashed black lines in those plots show the value of $dr/d\lambda$ for a dipole field. Gaps in the plots of the stretching parameter appear where the field has expanded too far down the tail to be evaluated or has run into the magnetopause.

The variation of the stretching parameter with rotation phase provides a way of quantifying the rotation phases at which magnetospheric expansion and contraction is significant at specific magnetospheric locations. Stretching is taken to start when the first upward change of $dr/d\lambda$ between consecutive points exceeds half the variance of $dr/d\lambda$ over one full cycle and to end at the maximum $dr/d\lambda$. Contraction begins at the maximum $dr/d\lambda$ and continues until the change of $dr/d\lambda$ between consecutive points falls below half the variance for at least three consecutive points without gaps. For example, at 3 LT at 10.5 R_S (Figure 10) a sharp change in slope of the $dr/d\lambda$ curve at about 90° indicates the onset of rapid stretching. The expansion peaks near 133° and the field collapses to roughly its initial configuration near 200° rotation phase. In contrast, in the same radial bin but at 21 LT, the expansion begins at 290° rotation phase, peaks at 123°, and ends near 216°. In the plots, blue shading indicates the range of rotation phase in which expansion is occurring locally, and red shading indicates where contraction is occurring.

At both 10.5 and 13.5 R_S, the field is stretched for a larger portion of a rotation period in the premidnight region than in the midnight or postmidnight region. Despite being stretched for a longer portion of a rotation period, the stretching parameter is considerably smaller premidnight than at midnight or postmidnight (e.g., at 10.5 R_S it reaches ~9 R_S/degree of invariant latitude premidnight, ~18 R_S/degree at midnight, and ~13 R_S/degree postmidnight). For the purposes of our analysis, we identify variations that occur inside of the colored shaded region as associated with both spinning and stretching and variations outside of the shaded region as imposed by spinning alone.

4.5. Separating Spinning and Breathing on the Nightside

Having found a way to characterize magnetospheric stretching as a function of LT and radial distance in the simulation, we attempt to identify which changes arise from spinning and which are dominated by breathing. This can be done only approximately, but we believe that the approach we next describe is meaningful. We model variations arising from spinning as sinusoidal functions of rotation phase. The magnetic pressure appears to rotate almost rigidly in the equatorial cuts of the simulation magnetosphere so a sinusoid should provide a good fit to the variations. However, we know from *Andrews et al*. [2010a, 2010b] that the peak phase of the magnetic field changes between radial bins. Therefore, we fit a sinusoid to the unstretched portion of the curve representing magnetic pressure in each radial and LT bin to identify the phases of extrema of spinning perturbations. The extrema in the magnetic pressure perturbations fall between 235° and 256° and between 55° and 76° depending on the radial distance in question. We postulate that these spin phases approximate extrema of the spinning contribution to the other parameters that we are trying to interpret. (We consider extrema in order to allow responses in the plasma to be close to in phase or out of phase with the magnetic perturbations.) The meridional flow in the simulated ionosphere peaks at 70° and 250°.

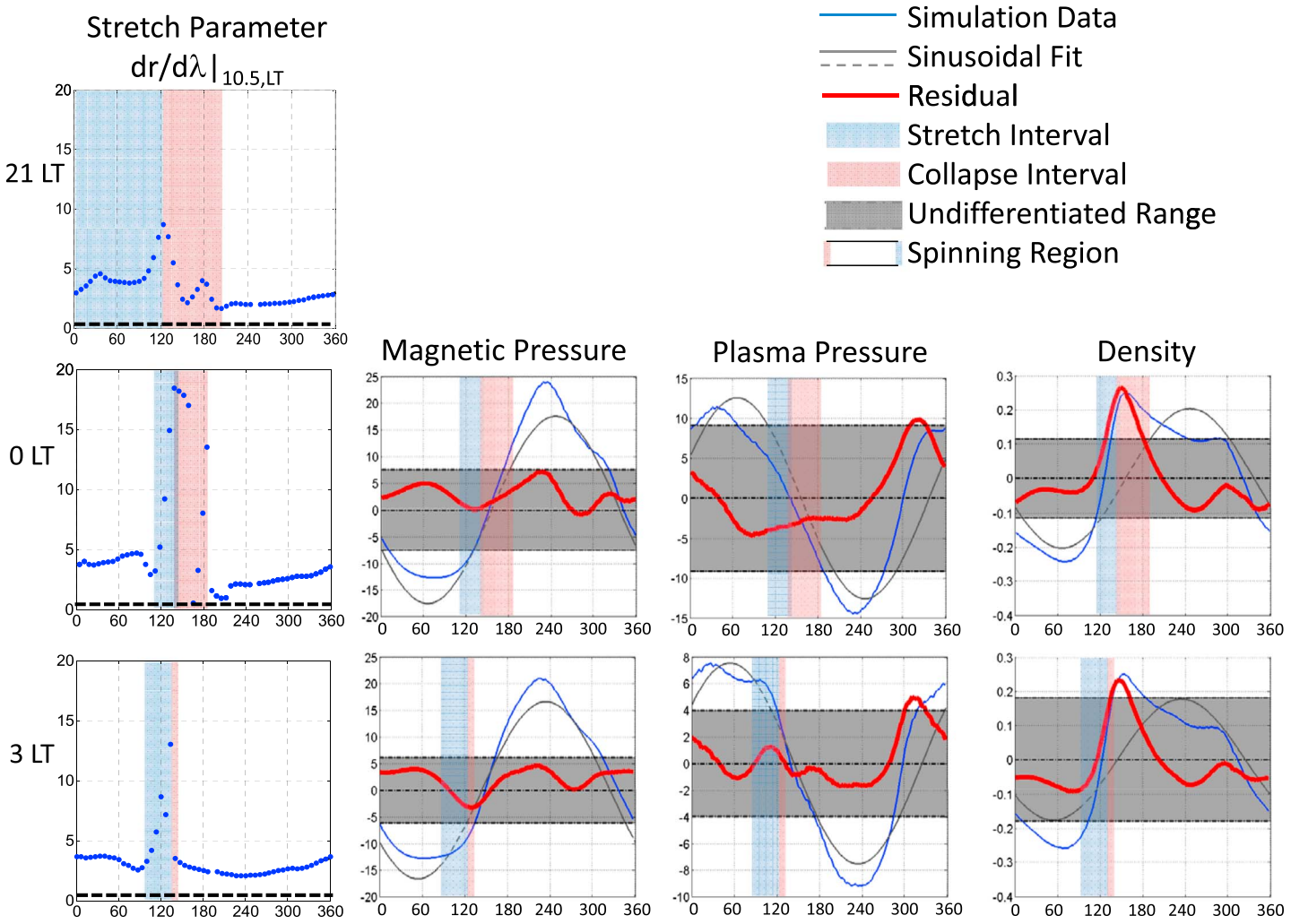

Figure 10. Plots of (first column) $dr/d\lambda$, (second column) magnetic pressure (pPa), (third column) plasma pressure (pPa), and (fourth column) density (#-cm^{-3}) perturbations at 10.5 R_S. Successive rows apply at different LTs (2100, 0000, and 0300). In the first column, containing the stretching proxy, stretching and relaxing regions (see text) are marked with blue and red shading, respectively. The expanding region (blue) begins when $dr/d\lambda$ begins to increase abruptly as a function of λ and ends at the maximum $dr/d\lambda$. The contracting region (red) begins at the maximum $dr/d\lambda$ and ends when $dr/d\lambda$ versus λ flattens. The shaded regions have been copied to the plots of the magnetic pressure, plasma pressure, and density. In these plots, the blue traces correspond to the waveform from the simulation at the specified LT and radial distance. The gray lines are sinusoidal fits to the unstretched region, with extrema specified by a fit to the magnetic pressure in each bin. The fit lines are solid in the unstretched region used for the fit and dashed otherwise. The heavy red line is the difference between the blue and gray curves. The width of the gray shaded region is twice the RMS of the difference between the fit and the simulation data in the unstretched region and provides an estimate of the range of fluctuations that is not significant.

Therefore, the extrema identified in the magnetic field occur within 30 min of the strongest radial flows imposed by the rotating current system. The Alfvén travel time from the ionosphere to the equator ranges between 20 and 30 min between 7.5 and 13.5 R_S [*McAndrews et al.*, 2009]. These travel times are short compared with the 10.8 h period that we are analyzing, so the close links in phase between ionospheric and magnetospheric perturbations is plausible.

We next fit sinusoids with extrema fixed by the magnetic pressure to the spinning portion of each plasma parameter. At 21 LT, the range of phase not affected by stretching was too small to provide a meaningful estimate of the phases of extrema in magnetic pressure. Therefore, results in Figures 10 and 11 are shown at 0 LT and 3 LT for 10.5 R_S and 13.5 R_S, respectively. In these figures, blue and red shading have been overlaid on plots of the magnetic pressure, plasma pressure, and density fluctuations (solid blue lines) to identify intervals of expansion and compression inferred from the rate of change of the stretching parameter. The black lines are sinusoidal fits to the simulated signal over the part of the rotation in which no significant expansion or

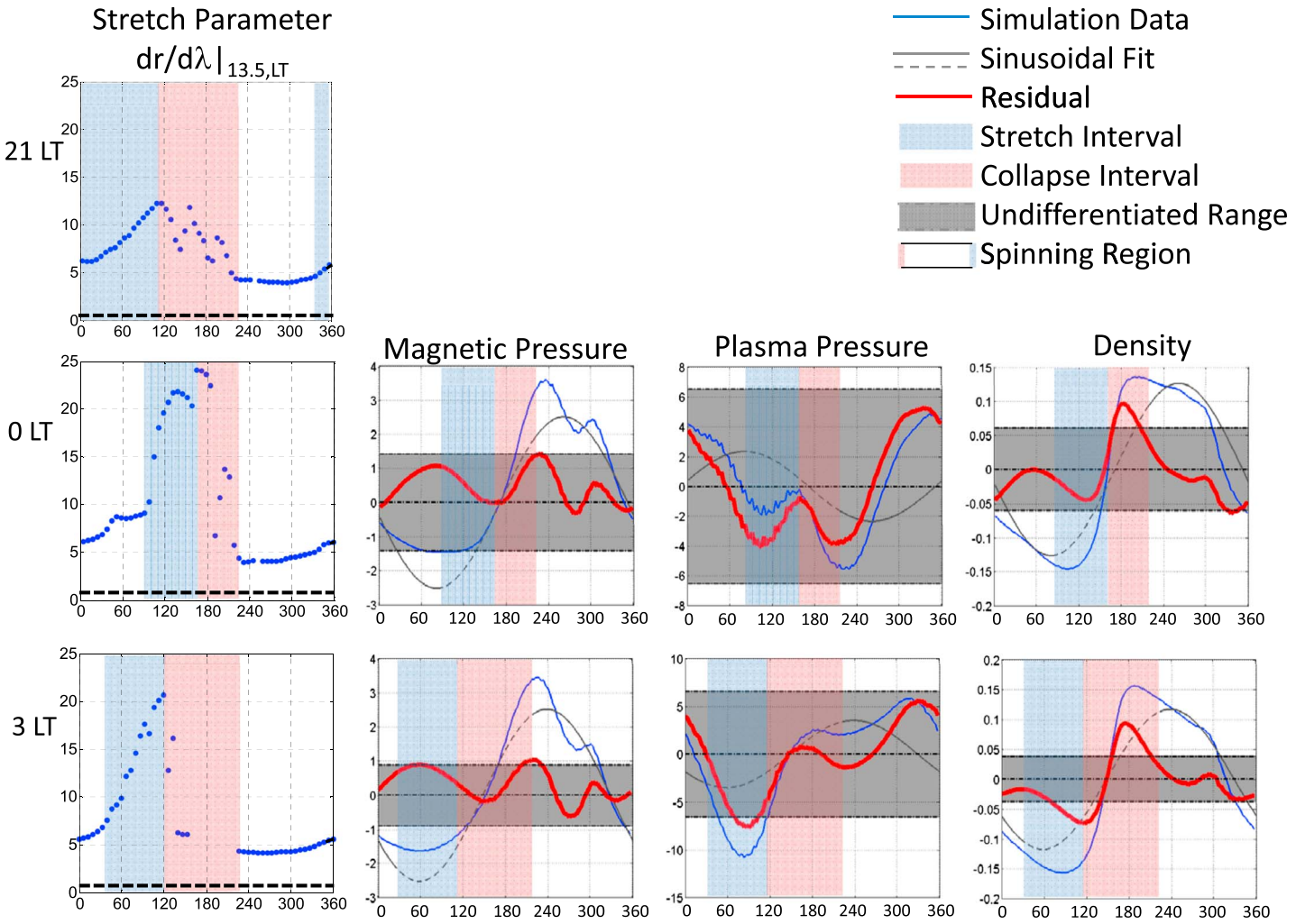

Figure 11. As for Figure 10, but for 13.5 R_S. At 3 LT, gaps appear in the dots of stretching parameter where field lines have reconnected or have hit the magnetopause. The unstretched region cannot contain gaps.

contraction is present, with the phases of the extrema specified by the magnetic pressure, as described above; the lines are drawn solid in the range of rotation phase used to fit the data and dashed elsewhere. In both Figures 10 and 11, the red lines, which we will refer to as residual perturbations, are the differences between the curves from the simulation and the sinusoidal fit. In order to estimate the scale of fluctuations unrelated to either spinning or breathing, we evaluate the RMS variations of the red curves in the spinning region. Portions of the red curves within 2 RMS of zero, shaded in dark gray in the plots, are regarded as insignificant because their variation is comparable with background fluctuations. We focus on the portions of the residual curves (red) that fall outside the shaded range which we believe are meaningfully related to breathing. We next interpret the results.

5. Discussion

We have previously remarked that periodic variations in magnetic pressure are dominated by the spinning response. At 10.5 (Figure 10), the sinusoids fit the spinning region very well and the residuals are of the order of the random fluctuations, indicating that the breathing response has little effect on the waveform of the magnetic pressure perturbations. At 13.5 R_S (Figure 11), the residuals meander beyond the shaded region both at midnight and 0300 LT at a rotation phase for which the tail is stretched but flux tubes are compressed azimuthally. This analysis reveals that the breathing response can modify the waveform of the magnetic

pressure in the outer part of the region we analyze. Thus, we confirm that the magnetic pressure perturbations on the nightside inside of 12 R_S are primarily controlled by spinning, but outside of 12 R_S, breathing alters the waveform as the field lines stretch and collapse.

Interpreting the role of the breathing response is more complicated for the plasma parameters. As the tail stretches, the plasma spreads radially, thereby reducing its density, but increasing stress due to rotation may compress plasma along the field lines toward the equatorial plane, an effect that increases the equatorial density. Changing field magnitude can heat or cool the plasma and thereby affect the thermal pressure. Thus, during intervals of stretch and collapse, it is hard to predict whether density and plasma pressure will increase or decrease as a result of stretching at any given local time or radial distance. What is evident, however, is that for the plasma parameters at both 10.5 and 13.5 R_S, significant excursions of the residual perturbations outside of the gray shaded regions occur only during stretched times. At 10.5 R_S, the residuals of the plasma pressure remain largely within the gray excluded region with excursions that are small compared to the size of the excluded range. Thus, although the range of uncertainty (gray shaded region) is a large fraction of the amplitude of the perturbation signature, we conclude that the plasma pressure perturbations at 10.5 R_S are imposed dominantly by spinning. At 13.5 R_S, the residual perturbation of the plasma pressure comes outside the excluded region inside of the stretched region at 3 LT. Although the size of the residual falling outside of the excluded region is small compared to the range of the excluded region, it is tempting to link this excursion to breathing because the decrease occurs when the tail is greatly stretched. Furthermore, the sinusoidal fits to the pressure at both midnight and 3 LT at 13.5 R_S are poor, suggesting that something is severely distorting the waveform from that related to pure spinning.

The waveforms of the residual density perturbations in all the LT and radial bins plotted display peaks that extend outside the gray region of uncertainty. In each case, the excursions fall inside of the stretched region, peaking at 10.5 R_S where stretching is maximum and at 13.5 R_S as the flux tubes are relaxing, strongly implying that the extended peak in density is due to the effects of breathing.

The simulation suggests how the stretching of the field lines may change the waveforms of the plasma and field parameters. The changes depend on which parameter is being considered and where the measurements are made. It is valuable then, to return to the data to determine whether our understanding applies to the real world.

The peak phase of the measured density perturbations, the bulk of which were taken on the dayside, was found to jump across some radial bins. We found similar behavior in the simulation and showed that periodic expansion and contraction of the magnetosphere can result in phase jumps across radial bins. Close to Saturn, the dominant effect of expansion is to increase the volume of flux tubes and decrease the plasma density, but outside of 9 R_S, as the plasma on stretched field lines moves farther from the planet, centrifugal forces not only move the plasma out but also accelerate the plasma along flux tubes toward the equator. The net effect in the stretched state can be to enhance the density in the equatorial plane outside of 9 R_S but depress it inside of 9 R_S. Thus, dayside breathing of the magnetosphere can account for the phase jump observed in the density data across radial bins.

In addition to creating phase shifts across radial bins, breathing can also cause phase shifts across local time bins. At 13.5 R_S, the plasma pressure in the simulation shifted phase by almost 180° across midnight. By examining the simulation, we found an asymmetry in the effects of stretching between premidnight and postmidnight. In the premidnight region, the magnetosphere stretches little, although it remains stretched for a large part of a rotation cycle. However, at midnight and postmidnight, the magnetosphere stretches more but over a shorter part of a rotation cycle. As a result, breathing imposes the peak phase of plasma pressure at midnight and postmidnight, but spinning seems to dominate breathing premidnight. Thus, the large shift in peak rotation phase for the plasma pressure from 12 to 15 R_S, can be attributed to the breathing of the nightside magnetosphere.

6. Summary and Conclusions

In this study, we set out to fit the ion plasma moments in the core magnetosphere inside of 15 R_S into the picture of the semirigidly rotating magnetosphere, a model that describes the magnetic field perturbations very well. We found that despite the scatter in the data, the measured equatorial plasma and field moments

from 6 to 15 R_S from October 2005 to August 2006, during southern summer, could be fitted by sinusoids modulated at the southern SKR period. However, the phases of peaks in the sinusoidal fits to the density and the thermal pressure of the plasma shifted across radial and local time bins in a way that was inconsistent with simple rotation. We used an MHD simulation by *Jia et al*. [2012] to put the observations into a global context. The simulation displays three types of large-scale periodic responses of the magnetosphere that we refer to as spinning (or rotating around the planet semirigidly), breathing (or compression and expansion of invariant latitude shells), and flapping (or the up and down motion of the current sheet). We found that the effects of flapping are negligible inside of 15 R_S. We used the radial displacement of the equatorial locations of invariant latitude magnetic shells in the simulation as a proxy for expansion and contraction of the magnetosphere and thereby identified the portion of the rotation period that was affected by breathing in different radial and local time bins. Breathing and spinning, both modulated at the southern SKR period, were found to act concurrently, but breathing was found to impose perturbations with different peak amplitudes and phases at different locations in the magnetosphere. The superposition of the two periodic variations accounted for the highly structured waveforms observed for simulated field and plasma properties at different radial distances and local times. Although the scatter in plasma measurements organized by rotation phase was too great to allow meaningful comparison with details of the structure of the rotation phase variations extracted from the simulation, their shifting maxima accounted for the shifting phases of maxima in the sinusoids fitted to measured plasma properties at different locations in the equatorial plane.

Our work shows that a single driver generating two different types of response at the same period can produce plasma perturbations that vary with rotation phase in ways that differ from the simple spinning that accounts for the variation of the magnetic perturbations in the core magnetosphere.

Acknowledgments

We thank Don Gurnett for providing the SLS4 phase used in this study. We thank Nick Sergis and Michelle Thomsen for initially providing us with the MIMI and CAPS data. We thank Raymond Walker and Robert J. Strangeway for many useful discussions. All data used in this study are publicly available via the NASA Planetary Data System with data set IDs of CO-E/SW/J/S-MAG-4-SUMM-1MINAVG-V1.0, CO-S-MIMI-4-CHEMS-CALIB-V1.0, CO-S-MIMI-4-LEMMS-CALIB-V1.0, and CO-E/J/S/SW-CAPS-5-DDR-ELE-MOMENTS-V1.0. This work was supported by NASA through grants NNX10AQ19G, NNX10AF16G, NNX11AK66G, and NNX13AL05G at UCLA. Xianzhe Jia acknowledges support by NASA through grant NNX12AK34G and the NASA Cassini mission under contract 1409449 with JPL. The simulation presented in this study was performed on the Pleiades supercomputer managed by the NASA advanced Supercomputing division.

References

Achilleos, N., P. Guio, C. S. Arridge, N. Sergis, R. J. Wilson, M. F. Thomsen, and A. J. Coates (2010), Influence of hot plasma pressure on the global structure of Saturn's magnetodisk, *Geophys. Res. Lett.*, *37*, L20201, doi:10.1029/2010GL045159.

Andrews, D. J., E. J. Bunce, S. W. H. Cowley, M. K. Dougherty, G. Provan, and D. J. Southwood (2008), Planetary period oscillations in Saturn's magnetosphere: Phase relation of equatorial magnetic field oscillations and Saturn kilometric radiation modulation, *J. Geophys. Res.*, *113*, A09205, doi:10.1029/2007JA012937.

Andrews, D. J., A. J. Coates, S. W. H. Cowley, M. K. Dougherty, L. Lamy, G. Provan, and P. Zarka (2010a), Magnetospheric period oscillations at Saturn: Comparison of equatorial and high-latitude magnetic field periods with north and south Saturn kilometric radiation periods, *J. Geophys. Res.*, *115*, A12252, doi:10.1029/2010JA015666.

Andrews, D. J., S. W. H. Cowley, M. K. Dougherty, and G. Provan (2010b), Magnetic field oscillations near the planetary period in Saturn's equatorial magnetosphere: Variation of amplitude and phase with radial distance and LT, *J. Geophys. Res.*, *115*, A04212, doi:10.1029/2009JA014729.

Arridge, C. S., K. K. Khurana, C. T. Russell, D. J. Southwood, N. Achilleos, M. K. Dougherty, A. J. Coates, and H. K. Leinweber (2008), Warping of Saturn's magnetospheric and magnetotail current sheets, *J. Geophys. Res.*, *113*, A08217, doi:10.1029/2007JA012963.

Arridge, C. S., et al. (2011), Periodic motion of Saturn's night-side plasma sheet, *J. Geophys. Res.*, *116*, A11205, doi:10.1029/2011JA016827.

Brandt, P. C., K. K. Khurana, D. G. Mitchell, N. Sergis, K. Dialynas, J. F. Carbary, E. C. Roelof, C. P. Paranicas, S. M. Krimigis, and B. H. Mauk (2010), Saturn's periodic magnetic field perturbations caused by a rotating partial ring current, *Geophys. Res. Lett.*, *37*, L22103, doi:10.1029/2010GL045285.

Cao, H., C. T. Russell, U. R. Christensen, M. K. Dougherty, and M. E. Burton (2011), Saturn's very axisymmetric magnetic field: No secular variation or tilt, *Earth Planet. Sci. Lett.*, *304*, 22–28, doi:10.1016/j.epsl.2011.02.035.

Carbary, J. F. (2013), Longitude dependences of Saturn's ultraviolet aurora, *Geophys. Res. Lett.*, *40*, 1902–1906, doi:10.1002/grl.50430.

Carbary, J. F., and D. G. Mitchell (2013), Periodicities in Saturn's magnetosphere, *Rev. Geophys.*, *51*, 1–30, doi:10.1002/rog.20006.

Carbary, J. F., D. G. Mitchell, P. Brandt, C. Paranicas, and S. M. Krimigis (2008), ENA periodicities at Saturn, *Geophys. Res. Lett.*, *35*, L07102, doi:10.1029/2009GL033230.

Carbary, J. F., D. G. Mitchell, S. M. Krimigis, and N. Krupp (2009), Dual periodicities in energetic electrons at Saturn, *Geophys. Res. Lett.*, *36*, L20103, doi:10.1029/2009GL040517.

Clarke, K. E., et al. (2006), Cassini observations of planetary-period oscillations of Saturn's magnetopause, *Geophys. Res. Lett.*, *33*, L23104, doi:10.1029/2006GL027821.

Clarke, K. E., D. J. Andrews, C. S. Arridge, A. J. Coates, and S. W. H. Cowley (2010a), Magnetopause oscillations near the planetary period at Saturn: Occurrence, phase, and amplitude, *J. Geophys. Res.*, *115*, A08209, doi:10.1029/2009JA014745.

Clarke, K. E., D. J. Andrews, A. J. Coates, S. W. H. Cowley, and A. Masters (2010b), Magnetospheric period oscillations of Saturn's bow shock, *J. Geophys. Res.*, *115*, A05202, doi:10.1029/2009JA015164.

Cowley, S. W. H., D. M. Wright, E. J. Bunce, A. C. Carter, M. K. Dougherty, G. Giampieri, J. D. Nichols, and T. R. Robinson (2006), Cassini observations of planetary-period magnetic field oscillations in Saturn's magnetosphere: Doppler shifts and phase motion, *Geophys. Res. Lett.*, *33*, L07104, doi:10.1029/2005GL025522.

Desch, M. D., and M. L. Kaiser (1981), Voyager measurement of the rotation period of Saturn's magnetic field, *Geophys. Res. Lett.*, *8*(3), 253–256, doi:10.1029/GL008i003p00253.

Dougherty, M. K., et al. (2004), The Cassini magnetic field investigation, *Space Sci. Rev.*, *114*(1–4), 331–383, doi:10.1007/s11214-004-1432-2.

Dougherty, M. K., et al. (2005), Cassini magnetometer observations during Saturn orbit insertion, *Science*, *307*(1266), doi:10.1126/science.1106098.

Gurnett, D. A., et al. (2005), Radio and plasma wave observations at Saturn from Cassini's approach and first orbit, *Science*, *307*, 1255, doi:10.1126/science.1105356.

Gurnett, D. A., A. M. Persoon, W. S. Kurth, J. B. Groene, T. F. Averkamp, M. K. Dougherty, and D. J. Southwood (2007), The variable rotation period of the inner region of Saturn's plasma disk, *Science*, *316*, 422, doi:10.1126/science.1138562.

Gurnett, D. A., A. Lecacheux, W. S. Kurth, A. M. Persoon, J. B. Groene, L. Lamy, P. Zarka, and J. F. Carbary (2009a), Discovery of a north-south asymmetry in Saturn's radio rotation period, *Geophys. Res. Lett.*, *36*, L16102, doi:10.1029/2009GL039621.

Gurnett, D. A., A. M. Persoon, J. B. Groene, A. J. Kopf, G. B. Hospodarsky, and W. S. Kurth (2009b), A north-south difference in the rotation rate of auroral hiss at Saturn: Comparison to Saturn's kilometric radio emission, *Geophys. Res. Lett.*, *36*, L21108, doi:10.1029/2009GL040774.

Gurnett, D. A., J. B. Groene, T. F. Averkamp, W. S. Kurth, S.-Y. Ye, and G. Fischer (2011), A SLS4 longitude system based on a tracking filter analysis of the rotational modulation of Saturn kilometric radiation, in *Planetary Radio Emissions VII*, edited by H. O. Rucker et al., Austrian Academy of Sciences Press, Vienna.

Jia, X., and M. G. Kivelson (2012), Driving Saturn's magnetospheric periodicities from the upper atmosphere/ionosphere: Magnetotail response to dual sources, *J. Geophys. Res.*, *117*, A11219, doi:10.1029/2012JA018183.

Jia, X., and M. G. Kivelson (2016), Dawn-dusk asymmetries in rotating magnetospheres: Lessons from modeling Saturn, *J. Geophys. Res. Space Physics*, *121*, 1413–1424, doi:10.1002/2015JA021950.

Jia, X., M. G. Kivelson, and T. I. Gombosi (2012), Driving Saturn's magnetospheric periodicities from the upper atmosphere/ionosphere, *J. Geophys. Res.*, *117*, A04215, doi:10.1029/2011JA017367.

Kaiser, M. L., M. D. Desch, J. W. Warwick, and J. B. Pierce (1980), Voyager detection of nonthermal radio emission from Saturn, *Science*, *209*, 1238, doi:10.1126/science.209.4462.1238.

Khurana, K. K., D. G. Mitchell, C. S. Arridge, M. K. Dougherty, C. T. Russell, C. Paranicas, N. Krupp, and A. J. Coates (2009), Sources of rotational signals in Saturn's magnetosphere, *J. Geophys. Res.*, *114*, A02211, doi:10.1029/2008JA013312.

Kivelson, M. G., and X. Jia (2014), Control of periodic variations in Saturn's maganetosphere by compressional waves, *J. Geophys. Res. Space Physics*, *119*, 8030–8045, doi:10.1002/2014JA020258.

Krimigis, S. M., et al. (2004), Magnetosphere Imaging Instrument (MIMI) on the Cassini mission to Saturn/Titan, *Space Sci. Rev.*, *114*, 233–329, doi:10.1007/s11214-004-1410-8.

Krimigis, S. M., N. Sergis, D. G. Mitchell, D. C. Hamilton, and N. Krupp (2007), A dynamic, rotating ring current around Saturn, *Nature*, *450*, 1050–1053, doi:10.1038/nature06425.

Kurth, W. S., A. Lecacheux, T. F. Averkamp, J. B. Groene, and D. A. Gurnett (2007), A Saturnian longitude system based on a variable kilometric radiation period, *Geophys. Res. Lett.*, *34*, L02201, doi:10.1029/2006GL028336.

Kurth, W. S., T. F. Averkamp, D. A. Gurnett, J. B. Groene, and A. Lecacheux (2008), An update to a Saturnian longitude system based on kilometric radio emissions, *J. Geophys. Res.*, *113*, A05222, doi:10.1029/2007JA012861.

Lamy, L. (2010), Variability of SKR north/south periods from short to long-term time scales, in *Proceedings of the 7th International Workshop on Planetary, Solar and Heliospheric Radio Emissions*, Graz, Austria, arXiv:1102.3099.

McAndrews, H. J., et al. (2009), Plasma in Saturn's nightside magnetosphere and the implications for global circulation, *Planet. Space Sci.*, *57*, 1714–1722, doi:10.1016/j.pss.2009.03.003.

Nichols, J. D., B. Cecconi, J. T. Clarke, S. W. H. Cowley, J.-C. Gérard, A. Grocott, D. Grodent, L. Lamy, and P. Zarka (2010a), Variation of Saturn's UV aurora with SKR phase, *Geophys. Res. Lett.*, *37*, L15102, doi:10.1029/2010GL044057.

Nichols, J. D., S. W. H. Cowley, and L. Lamy (2010b), Dawn-dusk oscillation of Saturn's conjugate auroral ovals, *Geophys. Res. Lett.*, *37*, L24102, doi:10.1029/2010GL045818.

Paranicas, C., D. G. Mitchell, S. Livi, S. M. Krimigis, E. Roussos, N. Krupp, J. Woch, A. Lagg, J. Saur, and F. S. Turner (2005a), Evidence of Enceladus and Tethys microsignatures, *Geophys. Res. Lett.*, *32*, L20101, doi:10.1029/2005GL024072.

Paranicas, C., D. G. Mitchell, E. C. Roelof, P. C. Brandt, D. J. Williams, S. M. Krimigis, and B. H. Mauk (2005b), Periodic intensity variations in global ENA images of Saturn, *Geophys. Res. Lett.*, *32*, L21101, doi:10.1029/2005GL023656.

Paranicas, C., et al. (2010), Asymmetries in Saturn's radiation belts, *J. Geophys. Res.*, *115*, A07216, doi:10.1029/2009JA014971.

Persoon, A. M., D. A. Gurnett, W. S. Kurth, and J. B. Groene (2006), A simple scale height model of the electron density in Saturn's plasma disk, *Geophys. Res. Lett.*, *33*, L18106, doi:10.1029/2006GL027090.

Pilkington, N. M., N. Achilleos, C. S. Arridge, P. Guio, A. Masters, L. C. Ray, N. Sergis, M. F. Thomsen, A. J. Coates, and M. K. Dougherty (2015), Internally driven large-scale changes in the size of Saturn's magnetosphere, *J. Geophys. Res. Space Physics*, *120*, 7289–7306, doi:10.1002/2015JA021290.

Provan, G., D. J. Andrews, C. S. Arridge, A. J. Coates, S. W. H. Cowley, S. E. Milan, M. K. Dougherty, and D. M. Wright (2009a), Polarization and phase of planetary-period magnetic field oscillations on high-latitude field lines in Saturn's magnetosphere, *J. Geophys. Res.*, *114*, A02225, doi:10.1029/2008JA013782.

Provan, G., S. W. H. Cowley, and J. D. Nichols (2009b), Phase relation of oscillations near the planetary period of Saturn's auroral oval and the equatorial magnetospheric magnetic field, *J. Geophys. Res.*, *114*, A04205, doi:10.1029/2008JA013988.

Provan, G., D. J. Andrews, B. Cecconi, S. W. H. Cowley, M. K. Dougherty, L. Lamy, and P. M. Zarka (2011), Magnetospheric period magnetic field oscillations at Saturn: Equatorial phase "jitter" produced by superposition of southern and northern period oscillations, *J. Geophys. Res.*, *116*, A04225, doi:10.1029/2010JA016213.

Provan, G., D. J. Andrews, C. S. Arridge, A. J. Coates, S. W. H. Cowley, G. Cox, M. K. Dougherty, and C. M. Jackman (2012), Dual periodicities in planetary-period magnetic field oscillations in Saturn's tail, *J. Geophys. Res.*, *117*, A01209, doi:10.1029/2011JA017104.

Roussos, E., et al. (2005), Low energy electron microsignatures at the orbit of Tethys: Cassini MIMI/LEMMS observations, *Geophys. Res. Lett.*, *32*, L24107, doi:10.1029/2005GL024084.

Sergis, N., S. M. Krimigis, D. G. Mitchell, D. C. Hamilton, N. Krupp, B. M. Mauk, E. C. Roelof, and M. Dougherty (2007), Ring current at Saturn: Energetic particle pressure in Saturn's equatorial magnetosphere measured with Cassini/MIMI, *Geophys. Res. Lett.*, *34*, L09102, doi:10.1029/2006GL029223.

Sergis, N., S. M. Krimigis, D. G. Mitchell, D. C. Hamilton, N. Krupp, B. H. Mauk, E. C. Roelof, and M. K. Dougherty (2009), Energetic particle pressure in Saturn's magnetosphere measured with the Magnetospheric Imaging Instrument on Cassini, *J. Geophys. Res.*, *114*, A02214, doi:10.1029/2008JA013774.

Sergis, N., et al. (2010), Particle pressure, inertial force, and ring current density profiles in the magnetosphere of Saturn, based on Cassini measurements, *Geophys. Res. Lett.*, *37*, L02102, doi:10.1029/2009GL041920.

Sergis, N., C. S. Arridge, S. M. Krimigis, D. G. Mitchell, A. M. Rymer, D. C. Hamilton, N. Krupp, M. K. Dougherty, and A. J. Coates (2011), Dynamics and seasonal variations in Saturn's magnetospheric plasma sheet, as measured by Cassini, *J. Geophys. Res.*, *116*, A04203, doi:10.1029/2010JA016180.

Smith, E. J., L. Davis Jr., D. E. Jones, P. J. Coleman Jr., D. S. Colburn, P. Dyal, and C. P. Sonett (1980), Saturn's magnetic field and magnetosphere, *Science*, *207*(407-410), doi:10.1126/science.207.4429.407.

Southwood, D. J. (1977), Localised compressional hydromagnetic waves in the magnetospheric ring current, *Planet. Space Sci.*, *25*, 549–554, doi:10.1016/0032-0633(77)90061-7.

Southwood, D. J., and M. G. Kivelson (2007), Saturnian magnetospheric dynamics: Elucidation of a camshaft model, *J. Geophys. Res.*, *112*, A12222, doi:10.1029/2007JA012254.

Thomsen, M. F., D. B. Reisenfeld, D. M. Delapp, R. L. Tokar, D. T. Young, F. J. Crary, E. C. Sittler, M. A. McGraw, and J. D. Williams (2010), Survey of ion plasma parameters in Saturn's magnetosphere, *J. Geophys. Res.*, *115*, A10220, doi:10.1029/2010JA015267.

Thomsen, M. F., E. Roussos, M. Andriopoulou, P. Kollmann, C. S. Arridge, C. P. Paranicas, D. A. Gurnett, R. L. Powell, R. L. Tokar, and D. T. Young (2012), Saturn's inner magnetospheric convection pattern: Further evidence, *J. Geophys. Res.*, *117*, A09208, doi:10.1029/2011JA017482.

Warwick, J. W., et al. (1981), Planetary radio astronomy observations from Voyager 1 near Saturn, *Science*, *212*, 4491, doi:10.1126/science.212.4491.239.

Wilson, R. J., F. Bagenal, P. A. Delamere, M. Desroche, B. L. Fleshman, and V. Dols (2013), Evidence from radial velocity measurements of a global electric field in Saturn's inner magnetosphere, *J. Geophys. Res. Space Physics*, *118*, 2122–2132, doi:10.1002/jgra.50251.

Yates, J. N., D. J. Southwood, and M. K. Dougherty (2015), Magnetic phase structure of Saturn's 10.7 h oscillations, *J. Geophys. Res. Space Physics*, *120*, 2631–2648, doi:10.1002/2014JA020629.

Young, D. T., et al. (2004), CAssini plasma spectrometer investigation, *Space Sci. Rev.*, *114*(1–4), 1–112, doi:10.1007/s11214-004-1406-4.